



**HAL**  
open science

## Trace elements discriminate between tissues in highly weathered fossils

Pierre Gueriau, Farid Saleh, Lukáš Laibl, Francesc Perez Peris, Lorenzo Lustri, Cristian Mocuta, Solenn Réguer, Serge X. Cohen, Loïc Bertrand, Allison C Daley

► **To cite this version:**

Pierre Gueriau, Farid Saleh, Lukáš Laibl, Francesc Perez Peris, Lorenzo Lustri, et al.. Trace elements discriminate between tissues in highly weathered fossils. 2023. hal-04230408

**HAL Id: hal-04230408**

**<https://hal.science/hal-04230408>**

Preprint submitted on 5 Oct 2023

**HAL** is a multi-disciplinary open access archive for the deposit and dissemination of scientific research documents, whether they are published or not. The documents may come from teaching and research institutions in France or abroad, or from public or private research centers.

L'archive ouverte pluridisciplinaire **HAL**, est destinée au dépôt et à la diffusion de documents scientifiques de niveau recherche, publiés ou non, émanant des établissements d'enseignement et de recherche français ou étrangers, des laboratoires publics ou privés.



Distributed under a Creative Commons Attribution 4.0 International License

# 1 **Trace elements discriminate between tissues in highly weathered** 2 **fossils**

3  
4 **Pierre Gueriau<sup>a,b,1</sup>, Farid Saleh<sup>a,1</sup>, Lukáš Laibl<sup>a,c,d</sup>, Francesc Perez Peris<sup>a</sup>, Lorenzo Lustri<sup>a</sup>,**  
5 **Cristian Mocuta<sup>e</sup>, Solenn Réguer<sup>e</sup>, Serge X. Cohen<sup>b</sup>, Loïc Bertrand<sup>f</sup>, and Allison C. Daley<sup>a,1</sup>**  
6

7 <sup>a</sup>Institute of Earth Sciences, University of Lausanne, Géopolis, CH-1015 Lausanne, Switzerland;

8 <sup>b</sup>Université Paris-Saclay, CNRS, ministère de la Culture, UVSQ, MNHN, Institut photonique  
9 d'analyse non-destructive européen des matériaux anciens, 91192, Saint-Aubin, France;

10 <sup>c</sup>Czech Academy of Sciences, Institute of Geology, Rozvojová 269, 165 00 Prague 6, Czech  
11 Republic;

12 <sup>d</sup>Institute of Geology and Palaeontology, Faculty of Science, Charles University, Albertov 6,  
13 Prague, 12843, Czech Republic;

14 <sup>e</sup>Synchrotron SOLEIL, l'Orme des Merisiers, Départementale 128, 91190 Saint-Aubin, France;

15 <sup>f</sup>Université Paris-Saclay, ENS Paris-Saclay, CNRS, Photophysique et Photochimie  
16 Supramoléculaires et Macromoléculaires, 91190 Gif-sur-Yvette, France.

17

18 <sup>1</sup>To whom correspondence may be addressed. Emails: pierre.gueriau@hotmail.fr,  
19 farid.nassim.saleh@gmail.com, or allison.daley@unil.ch

20

21 **Author Contributions:** P.G. and A.C.D. designed the research; P.G., F.S., L.La., F.P.P., L.Lu.  
22 C.M. and S.R. performed the research; P.G., C.M., S.R., S.X.C. and L.B. contributed new  
23 reagents/analytic tools; P.G., F.S., S.X.C. and L.B. analysed data; P.G. and F.S. wrote the paper  
24 with input from all authors.

25

26 **Keywords:** Ordovician | Fezouata Biota | synchrotron X-ray fluorescence | taphonomy | nervous  
27 system

28

29 **ORCID**

30 PG, 0000-0002-7529-3456; FS, 0000-0002-7529-3456; LLa, 0000-0001-9049-3811; FPP, 0000-  
31 0002-4526-9308; LLu, 0000-0002-8951-5160; CM, 0000-0001-5540-449X; SR, 0000-0002-7449-  
32 0503; SXC, 0000-0003-2435-2417; LB, 0000-0001-6622-9113; ACD, 0000-0001-5369-5879

33

34 **Abstract**

35 **Palaeontologists assess the affinities of fossils using either morphology-based phylogenetic**  
36 **analyses, possibly enhanced by the use of advanced imaging techniques, or the identification**  
37 **of remnants or derivatives of fossil organic molecules with high taxonomic specificity**  
38 **(“biomarkers”). However, these approaches are often of little use for the majority of fossils**  
39 **whose original morphology and chemistry have been severely altered or completely lost**  
40 **during decay, diagenesis and modern weathering. Here we show that the inorganic**  
41 **incorporation of trace elements during fossilization and diagenesis can be used to assess the**  
42 **affinity of highly altered fossils, constituting a powerful tool overlooked so far. This is**  
43 **illustrated by the study of a wide range of animals from the Early Ordovician Fezouata Shale**  
44 **(Tremadocian, Morocco) using synchrotron X-ray fluorescence major-to-trace elemental**  
45 **mapping. Although all fossils studied here have turned into iron oxides, spectral analyses**  
46 **reveal that their different tissue types (i.e. biomineralised, sclerotised, cuticularised, and**  
47 **internal tissues) can be distinguished on the basis of their trace element inventories. The**  
48 **resulting elemental classes and distributions allowed us to identify an enigmatic, highly**  
49 **weathered organism as a new stem euarthropod preserving remains of its nervous system.**

50

51 Elucidating the origin and evolutionary history of life relies on the accurate placing of organisms,  
52 extant and extinct, on the tree of life. This has historically been based upon anatomical similarities,  
53 with clades being identified by shared derived characteristics (synapomorphies) that can be traced  
54 to a most recent common ancestor and are not present in more distant groups and ancestors. For  
55 extant organisms, such phylogenetic/cladistic classifications were revolutionised by molecular  
56 biology, which utilizes differences and similarities in genetic sequences, predominately DNA and  
57 RNA, to build trees of evolutionary relationships. However, despite being successfully applied to  
58 recently extinct animals such as the giant moas from New Zealand<sup>1,2</sup> or the iconic mammoth<sup>3,4</sup>,  
59 these methods are of limited use for most fossil organisms, because observed rates of DNA  
60 degradation indicate that in samples older than 1.5 million years, DNA is either severely crosslinked  
61 or non-detectable<sup>5</sup> and the oldest ancient DNA ever extracted (from permafrost-preserved  
62 mammoth teeth) is 1.6 million years old<sup>4</sup>. Palaeontology has undergone its own revolution with the  
63 advent of 3D X-ray microtomography and more recently a series of advanced 2D imaging  
64 techniques, which reveal previously inaccessible or invisible anatomical information<sup>6-12</sup>. These  
65 techniques allow fossil anatomy to be described better than ever before, providing a wide range of  
66 new characters that have led to better resolution of phylogenetic analyses<sup>13-15</sup>. Furthermore,  
67 although DNA is not preserved in ancient fossils, remnants or derivatives of ancient biomolecules  
68 can survive in the geological record, associated to organically-preserved fossil remains or isolated  
69 within sedimentary rocks<sup>16-26</sup>. Some of these compounds represent biomolecular signatures (or  
70 “biomarkers”) diagnostic of particular (often broad) clades of organisms, and therefore represent a  
71 powerful complement to fossil anatomies in revealing the history of life<sup>20</sup>. Nonetheless, such  
72 approaches provide little new information when applied to the majority of fossils whose  
73 morphology and chemistry have substantially been altered during decay, burial, diagenesis and  
74 weathering. As a result, recent studies focus on relatively “unaltered” specimens while many other  
75 fossils remain enigmatic in their affinities. New tools and approaches accounting for and exploiting  
76 information loss/gain during the taphonomic history are needed to help deciphering the affinities of  
77 altered fossils<sup>20,27,28</sup>.

78 Here we report the major-to-trace elemental composition of 14 strongly weathered fossil  
79 animals, including various arthropods, annelids, sponges and an echinoderm, from the Early  
80 Ordovician (Tremadocian) Fezouata Shale of Morocco<sup>29,30</sup> using synchrotron-based X-ray  
81 fluorescence (XRF) mapping. In this Burgess Shale-type deposit, fossils were originally preserved  
82 as carbonaceous compressions and/or in authigenic minerals including pyrite<sup>31,32</sup>, before being  
83 extensively weathered by modern water circulations that led to the leaching of carbon from  
84 carbonaceous compressions, the oxidation of pyrite crystals into yellow, red to purple iron oxide

85 pseudomorphs, the deposition of new, poorly crystallised Fe-oxides in previously non-pyritised  
86 areas, and the dissolution of carbonates from the matrix and from the skeletal elements of animals  
87 such as echinoderms<sup>31–34</sup>. We consistently extracted mean XRF spectra from the tissues preserved  
88 in our fossils, as well as from their surrounding sedimentary matrix (see Figs. 1A–M, Table S1 and  
89 Figs. S1–S14 for location and details on the specimens and the selected areas, and methods for the  
90 XRF spectra extraction strategy). Linear discriminant analysis (LDA) was then applied to assess  
91 systematic variation in the major-to-trace elemental chemistry of different structure types (defined  
92 according to Saleh et al.<sup>35</sup>), i.e. between biomineralised, sclerotised, cuticularised, and internal  
93 tissues, and the sedimentary matrix. We further show the potential of this framework to interpret the  
94 anatomy of a highly weathered enigmatic organism from the Fezouata Biota.

95

96

## 97 **Results and Discussion**

98

### 99 **Highly weathered fossils preserve tissue-specific trace elemental chemistries.**

100 Our results show that although the fossils have all been extensively weathered to Fe-oxides (usually  
101 goethite, more rarely hematite, as determined by Raman spectroscopy), their biomineralised,  
102 sclerotised, cuticularised, and internal tissues can still be distinguished based on their trace element  
103 composition (Fig. 1N). Iron is naturally the main element composing the fossils (as Fe-  
104 oxyhydroxides), but it is also the main element probed by our analyses for the surrounding shale (as  
105 Fe-bearing clay minerals) because light elements and particularly silicon cannot be detected with  
106 the used setup (see Methods). All fossil tissues are, nevertheless, richer in Fe than the shale, and are  
107 also considerably enriched in As and Pb (Fig. 1O). The proximity of biomineralised and sclerotised  
108 tissues in the LDA plot indicates they have a similar elemental composition, only discriminated by a  
109 slight enrichment in Ti and Zn in biomineralised tissues, and in Fe, Cu, As and Pb in sclerotised  
110 tissues. Cuticularised tissues differ by strong depletions in Cu and As, as well as in Rb, Sr and Y.  
111 The only internal tissue available for study contains little to no Ni, Cu, Zn and Ga, and is the most  
112 depleted in Rb, Sr and Y. Note that no chemical inventory was collected for soft cellular outer  
113 tissues in direct contact with seawater (e.g. tentacles) as they were never found preserved in the  
114 Fezouata Biota<sup>32,35</sup>.

115

116

117

118

The specific chemical inventory for each type of tissues can be further confirmed considering that analysed fossils were found in numerous and distant (up to >30 km; Fig. S15) contemporaneous outcrops with different modern-weathering history<sup>31</sup>. This means that the chemical discrimination between different tissue types is not specific to a particular outcrop, and

119 tissue types can be chemically differentiated within the entire Fezouata Shale, because it was  
120 affected by broadly similar water circulation processes in the Draa valley<sup>32</sup>. The high concentrations  
121 and chemical speciation of the accessory metals imply that they have accumulated mainly through  
122 reactive transport during diagenesis –before the material reaches a stage of depercolation where the  
123 formation of specific fluid pathways and remineralisation blocks further uptake– rather than being  
124 originally present in the living organism (and persisting through geological times). Indeed, Cu, As,  
125 Pb, Ti and Zn concentrations in the 0.02–0.86 wt% range (see Table S2, and Methods for XRF  
126 quantification) are exceeding by one to several orders of magnitude those encountered in modern  
127 relatives of the Fezouata organisms, even when inhabiting environments heavily contaminated by  
128 terrestrial pollutants<sup>37,38</sup>. Furthermore, the most contrasting metal Cu is present in all investigated  
129 fossils as a Cu-carbonate compound (Fig. S16), which ubiquitous occurrence in such a wide range  
130 of organisms and tissues cannot be original, particularly considering that weathering led to the  
131 dissolution of carbonates from skeletal elements of animals such as echinoderms<sup>31–34</sup>. A description  
132 of the precise mechanisms responsible for such a diagenetic uptake (i.e. percolation, deposition,  
133 adsorption or substitution) is beyond the scope of the present work, but it clearly indicates that  
134 tissue-specific physico-chemical differences persisted long enough after decay and early  
135 mineralization to distinctly influence later elemental uptake, leading to elemental signatures that  
136 were retained (at least locally) after extensive subsequent weathering.

137

### 138 **Trace elemental composition can identify tissue types in enigmatic fossils.**

139 Building on this tissue-specific chemical inventory, we used XRF mapping and the obtained LDA  
140 classification to interpret the anatomy of an enigmatic, highly weathered organism (AA-FETB-OI-  
141 22; Figs. 2A, B). While it is particularly challenging to optically investigate this specimen owing to  
142 its poorly preserved state, the distributions of Fe (enriched in fossil tissues) (Fig. 2C) and to a larger  
143 extent Rb (depleted in most fossil tissues) allow us to distinguish the outline of the organism (Fig.  
144 2D), which does not include the entire brownish-purplish weathered surface. Chemically, we can  
145 distinguish two different types of tissues in this fossil: one depleted in Rb (Fig. 2D), and a central,  
146 3-mm wide tubular structure strongly enriched in Fe (Fig. 2C), optically yellowish and burgundy in  
147 colour, which extends anteriorly into a 28-mm long, yellowish and unsegmented slender appendage  
148 that curves along its length and tapers to a pointed end (Figs. 2B, C). We extracted mean XRF  
149 spectra from these two tissues and the sedimentary matrix (see Fig. 2C, Table S1 and Fig. S17 for  
150 location and details on the selected areas) and added them to our LDA classification (Fig. 2E). The  
151 matrix spectrum perfectly clusters with the matrix spectra from the other Fezouata fossils. The  
152 composition of the main body part clusters with that of cuticularised tissues. The anterior part of the

153 Fe-rich tubular structure, however, does not cluster with biomineralised, sclerotised or cuticularised  
154 tissues. Its central position is in proximity to the one data point from known internal tissue, making  
155 this the most likely tissue type for this tubular structure. The posterior part of this tubular structure,  
156 which is more burgundy in colour (Fig. 2B) and of different trace elemental composition (richer in  
157 Cu and Pb; Fig. 2F), plots distinctively from the anterior part, closer to the internal tissue point (Fig.  
158 S17), and may therefore represent the remains of another internal system. Note that the richer in  
159 iron the XRF spectra extracted from weathered matrix areas are the closer they plot to cuticularised  
160 tissues, following the fact that the shale matrix (clay and silica) is way less concentrated in iron than  
161 the fossil tissues (Fe-oxyhydroxides) (Fig. S17).

162 Using the elemental composition as a guide, a description of the overall anatomy of this  
163 animal can be made (Fig. 2G). The organism has a cuticularised, 11-mm wide, elongated and  
164 parallel-side trunk region, through which runs a central 3-mm wide band of internal tissues that  
165 extends into a 28-mm long slender, tapering and unsegmented appendage. The trunk region shows  
166 several faint discontinuous parallel lines that suggest the body was segmented and divided into a  
167 minimum of 6 body units. Laterally to the trunk outline, the cuticularised tissues extend outwards  
168 into poorly-defined wide lateral flaps that are rounded or roughly triangular in outline. This  
169 combination of anatomical features is very reminiscent of *Kerygmachela kierkegaardii*, a stem-  
170 group euarthropod from the Cambrian Sirius Passet Biota of Greenland<sup>39,40</sup>. An affinity for the  
171 Fezouata Shale organism similar to *K. kierkegaardii* would suggest that one of the pair of frontal  
172 appendages has not been preserved in the Fezouata organism, explaining the asymmetrical position  
173 of the one that is present. Regardless, due to the 40 Myr gap between the Sirius Passet and the  
174 Fezouata Shale, it is unlikely that the Fezouata organism belongs to the same taxon. In any case,  
175 stem euarthropod affinities for this organism increase the species richness of the Fezouata Biota.

176 A closer look at the regions of the specimen interpreted as internal tissues reveals anatomical  
177 detail that allows us to identify the organ systems that are present. Microscopic examination of the  
178 anterior yellowish region of the internal tissues reveals the presence, besides numerous rock  
179 fractures, of lateral extensions (Fig. 3A). A higher-resolution XRF map (25- $\mu$ m pixel size) further  
180 unveils four Fe-rich spherical structures organised antero-posteriorly, as well as another pair of two  
181 spherical structures, not as rich in Fe, positioned laterally to the first spherical structure and  
182 connected to it by an elbow duct (Figs. 3B,C). The only interpretation for such an arrangement of  
183 structures is that they represent four ganglia of the nervous system and a pair of lateral eyes,  
184 respectively (Fig. 3C,D). Although rare, the fossilisation of nervous tissues is being documented in  
185 a growing number of fossils<sup>40-49</sup>. It is explained by the presence of highly reactive biogenic Fe in  
186 the nervous system, which has been proposed to initiate selective pyritisation very rapidly during

187 early diagenesis while other tissues are still decaying<sup>50</sup>. Nonetheless, the undisputable identification  
188 of fossilised internal anatomical features as remains of nervous tissues may be challenging. Aria et  
189 al. proposed a set of criteria for their recognition, namely the consideration of the specimen  
190 topology, the morphoanatomical consistency, the taphonomic context and redundancy<sup>51</sup>. The  
191 remains observed in AA-FETB-OI-22 meet most of the proposed criteria: surface relief has been  
192 carefully considered, as shown in our interpretative drawing (Fig. 3C), especially as the Fe  
193 distribution probed by XRF is not limited to the surface (see Methods) allowing us to confidently  
194 distinguish between relief and fossilised remains; features are consistent with those described from  
195 closely-related fossils<sup>40</sup>; detailed knowledge of the taphonomy at the site<sup>31-35</sup> and the dorso-ventral  
196 plane of preservation associated with some 3D preservation uncovered by XRF ensure that  
197 taphonomic variations have been considered. We, however, acknowledge that the redundancy  
198 criterion is not met, but we argue that if our method could uncover such new features in a random  
199 specimen then more are expected to be discovered. The internal anatomical features preserved in  
200 the analysed specimen therefore represent the first remains of a nervous system ever reported from  
201 the Ordovician period. The other regions of the internal tubular structure that have a different  
202 chemistry (Fig. 2F) likely represent remains of other internal tissues or systems (Fig. 2G).

203

#### 204 **Towards a more exhaustive documentation of the history of life**

205 The identification, based upon the tissue-specific incorporation of inorganic minor and trace  
206 elements, of a stem euarthropod yielding remains of the nervous system from Fezouata extends both  
207 its biodiversity and the range of tissues that could be preserved there. It also illustrates the potential  
208 of novel uses of advanced spectro-imaging techniques to identify pivotal yet poorly preserved  
209 and/or highly weathered fossils such as lower stem euarthropods, which are neither biomineralised  
210 nor sclerotised and as such have a low fossilisation potential.

211 Tissue-specific chemistry is known to be a powerful tool for interpreting the soft tissue  
212 anatomy of exceptionally preserved fossils. This approach has been developed with XRF mapping  
213 of a wide range of vertebrates retaining organometallic compounds derived from the original  
214 melanin pigments<sup>52-54</sup>. Recently, the discovery that tissue-specific chemical signatures can persist in  
215 fossilised internal melanosomes (quite common in the fossil record) has even suggested that it could  
216 potentially be used to constrain the affinities of enigmatic fossil vertebrates<sup>55</sup>. Yet, such an approach  
217 is limited to literally exceptionally preserved fossils, i.e. retaining molecular and/or organelles  
218 remains, which have only been affected by limited diagenetic<sup>55-57</sup>. In the case of most other fossils,  
219 which only preserve hard parts (bones, shells, plates, ossicles, biomineralised cuticle), and  
220 occasionally soft parts replicated in minerals during fossilisation and/or, diagenesis, the use of XRF



221 mapping has been limited to acquiring chemical information and visualising anatomical features  
222 superficially hidden beneath the sample surface<sup>10,11,58-60</sup>. Our study unexpectedly shows that the  
223 combination of both the spatial and chemical information provided by elemental mapping with  
224 appropriate sampling and data processing can represent, for a given locality, a powerful toolkit to  
225 decipher the anatomy and affinities of poorly preserved and/or highly weathered soft-bodied fossils.  
226 Documenting new anatomical features completes our knowledge of past biodiversity and ecology,  
227 while uncovering hidden evolutionary patterns. As such, this approach holds great promise in  
228 allowing a detailed understanding of overlooked aspects of the history of life.

229

230

## 231 **Materials and Methods**

232 **Fossil specimens.** The studied material is housed in the collections of the Musée cantonal de  
233 Géologie de Lausanne (MGL), and of the Cadi-Ayyad University (Faculté des Sciences et  
234 Techniques, Guéliz), Marrakesh, Morocco. The MGL material was collected by authorised and  
235 academically recognised avocational Moroccan collector Mohamed Ben Moula and his family over  
236 the period of 2015 to 2016; A.C.D. worked in collaboration with them to collect the metadata  
237 associated with the collected fossils. Mohamed Ben Moula has a long-standing working relationship  
238 with several academics, has received the Mary Anning Award from the Palaeontological  
239 Association, and has a radiodont fossil named after him in honour of his great contribution to the  
240 field of palaeontology. The collection was purchased with funds from the University of Lausanne  
241 and the Swiss National Science Foundation, following all regulations for purchases. The material  
242 was transported to Casablanca and subjected to export approval by the Ministry of Energy, Mines  
243 and the Environment of the federal government of the Kingdom of Morocco and approved for  
244 shipment to Switzerland on 11.05.2017 (export permits curated with the collection). The material  
245 from the Marrakesh collection studied herein was loaned to the University Lyon 1 for study and will  
246 be returned to the Cadi-Ayyad University after study.

247 Details about the fossil specimens investigated herein (identification, inventory numbers,  
248 and localities) are given in Table S1. Precise locality information is curated with the specimens, and  
249 available upon request from the authors. Specimens were selected to represent a variety of taxa and  
250 tissue types, for which remains are thicker than 300  $\mu\text{m}$  to make sure that the elemental signal  
251 recorded using  $\mu\text{XRF}$  only comes from the fossil itself and not also from the underlying  
252 sedimentary matrix. Details about the scanning steps and dwell times used for each map, as well as  
253 about the areas from which spectra have been extracted are also given in Table S1.

254

255

256 **Elemental mapping.** Synchrotron micro X-ray fluorescence ( $\mu$ XRF) major-to-trace elemental  
257 mapping was performed at the DiffAbs beamline of the SOLEIL synchrotron source (France), using  
258 a monochromatic beam of 18 keV ( $\Delta E/E \sim 1-2 \times 10^{-4}$ ), selected for excitation of K-lines from  
259 phosphorus to yttrium and L-lines from cadmium to uranium. In order to map the specimen with a  
260 high lateral resolution, the beam was reduced down to a diameter of 50  $\mu\text{m}$  using a molybdenum  
261 pinhole. The sample was mounted on a scanner stage allowing 90 mm movements (in both  
262 horizontal and vertical directions) with micrometre accuracy, and orientated at  $45^\circ$  with respect to  
263 the incident beam. XRF was collected using a 4-element silicon drift detector (SDD, Vortex ME4,  
264 Hitachi High-Technologies Science America, Inc., total active area: 170  $\text{mm}^2$ ) oriented at  $90^\circ$  with  
265 respect to the incident beam, in the horizontal plane<sup>11</sup> in order to minimize the elastic (Thompson)  
266 scattering signal.

267 Two-dimensional spectral images, *i.e.* images for which each pixel is characterised by a full  
268 XRF spectrum, were collected *on the fly*<sup>61</sup> over the specimens at a 20–200  $\mu\text{m}$  lateral resolution  
269 with a 20–70 ms dwell time (effective counting time was 90% of the dwell time) depending on the  
270 samples (see Table S1 for the precise scanning steps and dwell times used for each map). Spectra  
271 were then reduced by summing intensities from the four elements of the XRF detector, and  
272 integrating intensities every 100 eV. All elemental distributions presented herein correspond to  
273 integrated intensities from the main XRF peaks, produced using ImageJ and represented using grey,  
274 RGB composite or Green Fire Blue colour scales.

275

276 **XRF spectra extraction.** Based on the obtained elemental distributions, we consistently extracted  
277 mean XRF spectra from the different tissues preserved in our fossils, as well as from their  
278 surrounding sedimentary matrix, carefully selecting homogeneous areas (see Figs. 1A–M, Table S1  
279 and Figs. S1–S14 for location and details on the specimens and the selected areas). We particularly  
280 avoided Mn-rich areas that resulted from recent weathering and covered parts of some fossils (Figs.  
281 1D, G and L) as they would obscure other chemical signals; weathering in the Fezouata Shale was  
282 also responsible for the leaching of carbon, oxidation of pyrite, deposition of Fe-oxides and  
283 dissolution of carbonates<sup>31–34</sup>. To compensate for the use of different exposure times between  
284 datasets, the number of pixels for each area was adapted such that the collection time (and  
285 consequently the signal-to-noise ratio) was similar between all extracted spectra (see Table S1).  
286 Another important parameter to consider is the thickness of the fossil material. At 18 keV, the  
287 attenuation length for goethite (the main iron oxyhydroxide in the Fezouata fossils) is about 80  $\mu\text{m}$ :  
288 it is therefore essential that extracted spectra are collected from fossil tissues thicker than this

289 length, so that the extracted signal is not the sum of contributions from the fossil and the underlying  
290 sediment.

291

292 **Linear discriminant analyses.** Differences in elemental abundances between the tissue types of the  
293 14 identified fossils were assessed using a linear discriminant analysis (LDA), a method that  
294 explains (and predicts) the affiliation of an individual to a predefined class (group) based on the  
295 measured predictive variable characteristics. The analyses were performed in the R statistical  
296 environment using the `MASS` package<sup>62</sup>, and plotted using the `ggplot2` package<sup>63</sup>. The statistical  
297 analysis is based on the integrated intensity of the XRF signals of the different elements, with  
298 partial reabsorption by the matrix. To discriminate between tissues, we directly rely on the fact that  
299 the signal results from the statistical realisation of the photon-matter interaction (rather than  
300 quantitative estimates). Discrimination therefore takes into account both the average content in each  
301 element and its local distribution within each probed voxel (containing material of varying  
302 composition). Prior to the LDA, bending followed by a rubberband baseline corrections were  
303 applied to the log-normalised spectra using the `wl.eval` and `spc.rubberband` function of the  
304 `hyperSpec` package<sup>64</sup>. Spectra from the enigmatic organism were then added to the LDA plot  
305 using the `predict` function. Spectra and the R script used in this work are available via the  
306 following Dryad Digital Repository:

307 [https://datadryad.org/stash/share/LGEGhXAwq2FZjiD12k9MPFfZ1D0Vt0Z\\_M1wLWXSKzSw](https://datadryad.org/stash/share/LGEGhXAwq2FZjiD12k9MPFfZ1D0Vt0Z_M1wLWXSKzSw)  
308 (private, randomized URL for Peer Review until the related manuscript has been accepted).

309

310 **XRF quantification.** Full quantification of trace elements from XRF maps of heterogeneous  
311 materials such as fossils is generally hampered by local heterogeneity (both laterally and in depth),  
312 which limits the precision of corrections for matrix X-ray reabsorption, with strong impact on the  
313 calculated concentrations depending on the hypothesis on the matrix composition. Nonetheless, by  
314 carefully selecting homogeneous areas (based on elemental distributions) and defining the matrix,  
315 statistics are sufficient to estimate semi-quantitative contents of trace elements in fossils<sup>65,66</sup>. We  
316 estimated elemental concentrations in our fossils from a full spectral decomposition performed with  
317 the PyMCA data analysis software<sup>67</sup> using an Hypermet peak shape, a polynomial approximation of  
318 the baseline and experimental parameters, applying reabsorption corrections considering a goethite  
319 matrix (as determined by Raman spectroscopy). The photon flux was estimated to  $3.4 \times 10^9$   
320 photons $\cdot$ s<sup>-1</sup> taking Fe as internal standard (62.85wt% in pure goethite). Resulting concentrations  
321 expressed as wt% are presented in Table S2.

322

323 **Acknowledgments**

324 We are grateful to SOLEIL synchrotron for provision of beamtime, D. Thiaudière, and P. Joly for  
325 assistance at the DiffAbs beamline, as well as B. Lefebvre and E. Robert for facilitating access to  
326 the material from the Marrakesh collection, and G. Potin for help with the Musée cantonal de  
327 Géologie de Lausanne collection. P.G., F.P.P., L.Lu. and this research were funded by the Swiss  
328 National Science Foundation, grant number 205321\_179084 entitled “Arthropod Evolution during  
329 the Ordovician Radiation: Insights from the Fezouata Biota” and awarded to A.C.D. L.La. was  
330 supported by the Center for Geosphere Dynamics (UNCE/SCI/006), and by the institutional support  
331 RVO 67985831 of the Institute of Geology of the Czech Academy of Sciences. F.S. acknowledges  
332 funding from the Faculty of Geosciences and Environment of the University of Lausanne.

333

334

335 **References**

- 336 1. A. Cooper, C. Mourer-Chauviré, G. K. Chambers, A. von Haeseler, A. C. Wilson, S. Pääbo,  
337 Independent origins of New Zealand moas and kiwis. *Proc. Natl. Acad. Sci. U.S.A.* **89**,  
338 8741-8744 (1992).
- 339 2. A. J. Baker, L. J. Huynen, O. Haddrath, C. D. Millar, D. M. Lambert, Reconstructing the  
340 tempo and mode of evolution in an extinct clade of birds with ancient DNA: the giant moas  
341 of New Zealand. *Proc. Natl. Acad. Sci. U.S.A.* **102**, 8257-8262 (2005).
- 342 3. R. Debruyne, V. Barriel, P. Tassy, Mitochondrial cytochrome *b* of the Lyakhov mammoth  
343 (Proboscidea, Mammalia): new data and phylogenetic analyses of Elephantidae. *Mol.*  
344 *Phylogenet. Evol.* **26**, 421–434 (2003).
- 345 4. T. van der Valk, P. Pečnerová, D. Díez-del-Molino, A. Bergström, J. Oppenheimer *et al.*  
346 Million-year-old DNA sheds light on the genomic history of mammoths. *Nature* **591**, 265–  
347 269 (2021).
- 348 5. E. Willerslev, A. J. Hansen, R. Rønn, T. B. Brand, I. Barnes, C. Wiuf, D. Gilichinsky, D.  
349 Mitchell, A. Cooper, Long-term persistence of bacterial DNA. *Curr. Biol.* **14**, R9–R10  
350 (2004).
- 351 6. P. Tafforeau, R. Boistel, E. Boller, A. Bravin, M. Brunet *et al.*, Applications of X-ray  
352 synchrotron microtomography for non-destructive 3D studies of paleontological specimens.  
353 *Appl. Phys. A* **83**, 195–202 (2006).
- 354 7. S. Y. Smith, M. E. Collinson, P. J. Rudall, D. A. Simpson, F. Marone, M. Stampanoni,  
355 Virtual taphonomy using synchrotron tomographic microscopy reveals cryptic features and  
356 internal structure of modern and fossil plants. *Proc. Natl. Acad. Sci. U.S.A.* **106**, 12013-  
357 12018 (2009).
- 358 8. U. Bergmann, R. W. Morton, P. L. Manning, W. I. Sellers, S. Farrar, K. G. Huntley, R. A.  
359 Wogelius, P. L. Larson, *Archaeopteryx* feathers and bone chemistry fully revealed via  
360 synchrotron imaging. *Proc. Natl. Acad. Sci. U.S.A.* **107**, 9060–9065 (2010).
- 361 9. U. Bergmann, L. Bertrand, N. P. Edwards, P. L. Manning, R. A. Wogelius, “Chemical  
362 mapping of ancient artifacts and fossils with x-ray spectroscopy” in *Synchrotron Light*

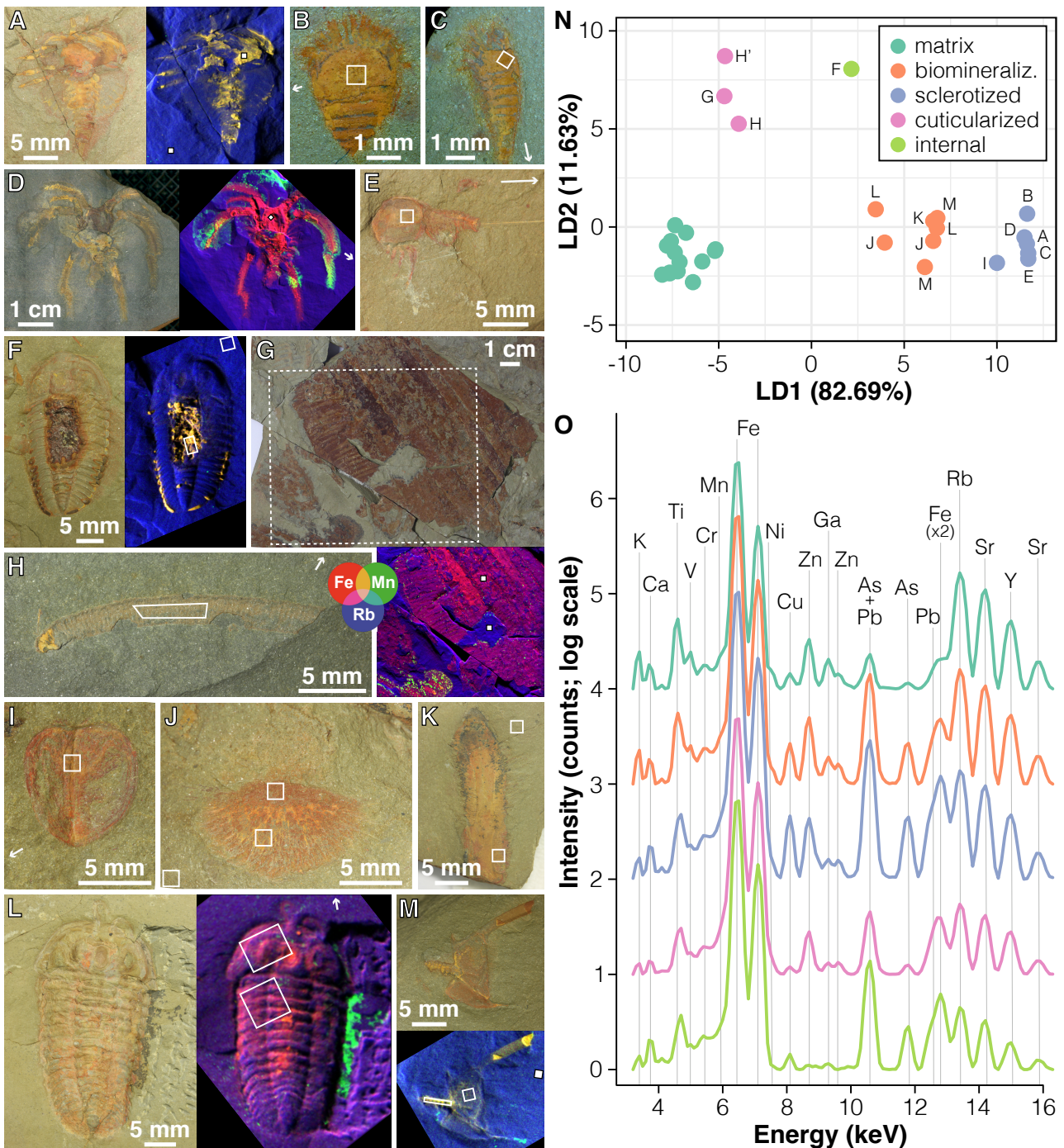
- 363 *Sources and Free-Electron Lasers: Accelerator Physics, Instrumentation and Science*  
364 *Applications*, E. Jaeschke, S. Khan, J. R. Schneider, J. B. Hastings, Eds. (Springer Nature  
365 Switzerland, 2019).
- 366 10. P. Gueriau, C. Mocuta, D. B. Dutheil, S. X. Cohen, D. Thiaudière, The OT1 Consortium, S.  
367 Charbonnier, G. Clément, L. Bertrand, Trace elemental imaging of rare earth elements  
368 discriminates tissues at microscale in flat fossils. *PLoS One* **9**, e86946 (2014).
- 369 11. P. Gueriau, C. Jauvion, C. Mocuta, Show me your yttrium, and I will tell you who you are:  
370 implications for fossil imaging. *Palaeontology* **61**, 981–990 (2018).
- 371 12. T. G. Kaye, A. R. Falk, M. Pittman, P. C. Sereno, L. D. Martin, D. A. Burnham, E. Gong, X.  
372 Xu, Y. Wang, Laser-Stimulated Fluorescence in Paleontology. *PLoS One* **10**, e0125923  
373 (2015).
- 374 13. S. Giles, M. Friedman, M. Brazeau, Osteichthyan-like cranial conditions in an Early  
375 Devonian stem gnathostome. *Nature* **520**, 82–85 (2015).
- 376 14. D. Zhai, J. Ortega-Hernández, J. M. Wolfe, X. Hou, C. Cao, Y. Liu, Three-dimensionally  
377 preserved appendages in an Early Cambrian stem-group pancrustacean. *Curr. Biol.* **29**, 171–  
378 177 (2019).
- 379 15. T. Miyashita, M. I. Coates, R. Farrar, P. Larson, P. L. Manning, R. A. Wogelius, N. P.  
380 Edwards, J. Anné, U. Bergmann, A. R. Palmer, P. J. Currie, Hagfish from the Cretaceous  
381 Tethys Sea and a reconciliation of the morphological–molecular conflict in early vertebrate  
382 phylogeny. *Proc. Natl. Acad. Sci. U.S.A.* **116**, 2146–2151 (2019).
- 383 16. J. J. Brocks, R. E. Summons, Sedimentary Hydrocarbons. *Biogeochemistry* **8**, 63–115  
384 (2005).
- 385 17. J. J. Brocks, A. Pearson, Building the biomarker tree of life. *Rev. Mineral. Geochem.* **59**,  
386 233–258 (2005).
- 387 18. J. Lindgren, P. Uvdal, P. Sjövall, D. E. Nilsson, A. Engdahl *et al.*, Molecular preservation of  
388 the pigment melanin in fossil melanosomes. *Nat. Communications* **3**, 824 (2012).
- 389 19. D. E. Greenwalt, Y. S. Goreva, S. M. Siljeström, T. Rose, R. E. Harbach, Hemoglobin-  
390 derived porphyrins preserved in a Middle Eocene blood-engorged mosquito. *Proc. Natl.*  
391 *Acad. Sci. U.S.A.* **110**, 18496–18500 (2013).
- 392 20. D. E. G. Briggs, R. Summons, Ancient biomolecules: their origins, fossilization, and role in  
393 revealing the history of life. *BioEssays* **36**, 482–490 (2014).
- 394 21. C. Colleary, A. Dolocan, J. Gardner, S. Singh, M. Wuttke *et al.*, Chemical, experimental,  
395 and morphological evidence for diagenetically altered melanin in exceptionally preserved  
396 fossils. *Proc. Natl. Acad. Sci. U.S.A.* **112**, 12592–12597 (2015).
- 397 22. Y. Pan, W. Zheng, A. E. Moyer, J. K. O’Connor, M. Wang *et al.*, Molecular evidence of  
398 keratin and melanosomes in feathers of the Early Cretaceous bird *Eoconfuciusornis*. *Proc.*  
399 *Natl. Acad. Sci. U.S.A.* **113**, E7900–E7907 (2016).
- 400 23. V. Vajda, M. Pucetaite, S. McLoughlin, A. Engdahl, J. Heimdal, P. Uvdal, Molecular  
401 signatures of fossil leaves provide unexpected new evidence for extinct plant relationships.  
402 *Nat. Ecol. Evol.* **1**, 1093–1099 (2017).
- 403 24. I. Bobrovskiy, J. M. Hope, A. Ivantsov, B. J. Nettersheim, C. Hallmann, J. J. Brocks,  
404 Ancient steroids establish the Ediacaran fossil *Dickinsonia* as one of the earliest animals.  
405 *Science* **361**, 1246–1249 (2018).

- 406 25. Y. Pan, W. Zheng, R. H. Sawyer, M. W. Pennington, X. Zheng *et al.*, The molecular  
407 evolution of feathers with direct evidence from fossils. *Proc. Natl. Acad. Sci. U.S.A.* **116**,  
408 3018–3023 (2019).
- 409 26. K. H. Kjær, M. Winther Pedersen, B. De Sanctis, B. De Cahsan, T. S. Korneliussen *et al.*, A  
410 2-million-year-old ecosystem in Greenland uncovered by environmental DNA. *Nature* **612**,  
411 283–291 (2022).
- 412 27. D. J. Murdock, S. E. Gabbott, M. A. Purnell M.A., The impact of taphonomic data on  
413 phylogenetic resolution: *Helenodora inopinata* (Carboniferous, Mazon Creek Lagerstätte)  
414 and the onychophoran stem lineage. *BMC Evol. Biol.* **16**, 19 (2016).
- 415 28. L. Bertrand, M. Thoury, P. Gueriau, É. Anheim, S. Cohen, Deciphering the Chemistry of  
416 Cultural Heritage: Targeting Material Properties by Coupling Spectral Imaging with Image  
417 Analysis. *Acc. Chem. Res.* **54**, 19670–19676 (2021).
- 418 29. P. Van Roy, P. J. Orr, J. P. Botting, L. A. Muir, J. Vinther, B. Lefebvre, K. El Hariri, D. E.  
419 G. Briggs, Ordovician faunas of Burgess Shale type. *Nature* **465**, 215–218 (2010).
- 420 30. P. Van Roy, D. E. G. Briggs, R. R. Gaines, The Fezouata fossils of Morocco; an  
421 extraordinary record of marine life in the Early Ordovician. *J. Geol. Soc.* **172**, 541–549  
422 (2015).
- 423 31. F. Saleh, B. Pittet, P. Sansjofre, P. Gueriau, S. Lalonde *et al.*, Taphonomic pathway of  
424 exceptionally preserved fossils in the Lower Ordovician of Morocco. *Geobios* **60**, 99–115  
425 (2020).
- 426 32. F. Saleh, R. Vaucher, J. B. Antcliffé, A. C. Daley, K. El Hariri *et al.*, Insights into soft-part  
427 preservation from the Early Ordovician Fezouata Biota. *Earth-Science Reviews* **213**, 103464  
428 (2021).
- 429 33. B. Lefebvre, T. E. Guensburg, E. L. O. Martin, R. Mooi, E. Nardin *et al.*, Exceptionally  
430 preserved soft parts in fossils from the Lower Ordovician of Morocco clarify stylophoran  
431 affinities within basal deuterostomes. *Geobios* **52**, 27–36 (2019).
- 432 34. F. Saleh, B. Lefebvre, A. W. Hunter, M. Nohejlov, Fossil weathering and preparation mimic  
433 soft tissues in eocrinoid and somasteroid echinoderms from the Lower Ordovician of  
434 Morocco. *Microscopy today* **28**, 24–28 (2020).
- 435 35. F. Saleh, J. B. Antcliffé, B. Lefebvre, B. Pittet, L. Laibl *et al.*, Taphonomic bias in  
436 exceptionally preserved biotas. *Earth and Planetary Science Letters* **529**, 115873 (2020).
- 437 36. P. Brouwer, *Theory of XRF* (PANalytical B.V., Almelo, The Netherlands, 2006).
- 438 37. J. Burger, C. Dixon, T. Shukla, N. Tsipoura, M. Gochfeld, Metal levels in horseshoe crabs  
439 (*Limulus polyphemus*) from Maine to Florida. *Environmental research* **90**, 227–236 (2002).
- 440 38. Q. Liu, X. Xu, J. Zeng, X. Shi, Y. Liao *et al.*, Heavy metal concentrations in commercial  
441 marine organisms from Xiangshan Bay, China, and the potential health risks. *Marine*  
442 *pollution bulletin* **141**, 215–226 (2019).
- 443 39. G. B. Budd, A Cambrian gilled lobopod from Greenland. *Nature* **364**, 709–711 (1993).
- 444 40. T.-Y. S. Park, J.-H. Kihm, J. Woo, C. Park, W. Y. Lee, M. P. Smith, D. A. T. Harper, F.  
445 Young, A. T. Nielsen, J. Vinther, Brain and eyes of *Kerygmachela* reveal protocerebral  
446 ancestry of the panarthropod head. *Nature Communications* **9**, 1019 (2018).
- 447 41. X. Ma, X. Hou, G. D. Edgecombe, N. J. Strausfeld, Complex brain and optic lobes in an  
448 early Cambrian arthropod. *Nature* **490**, 258–261 (2012).

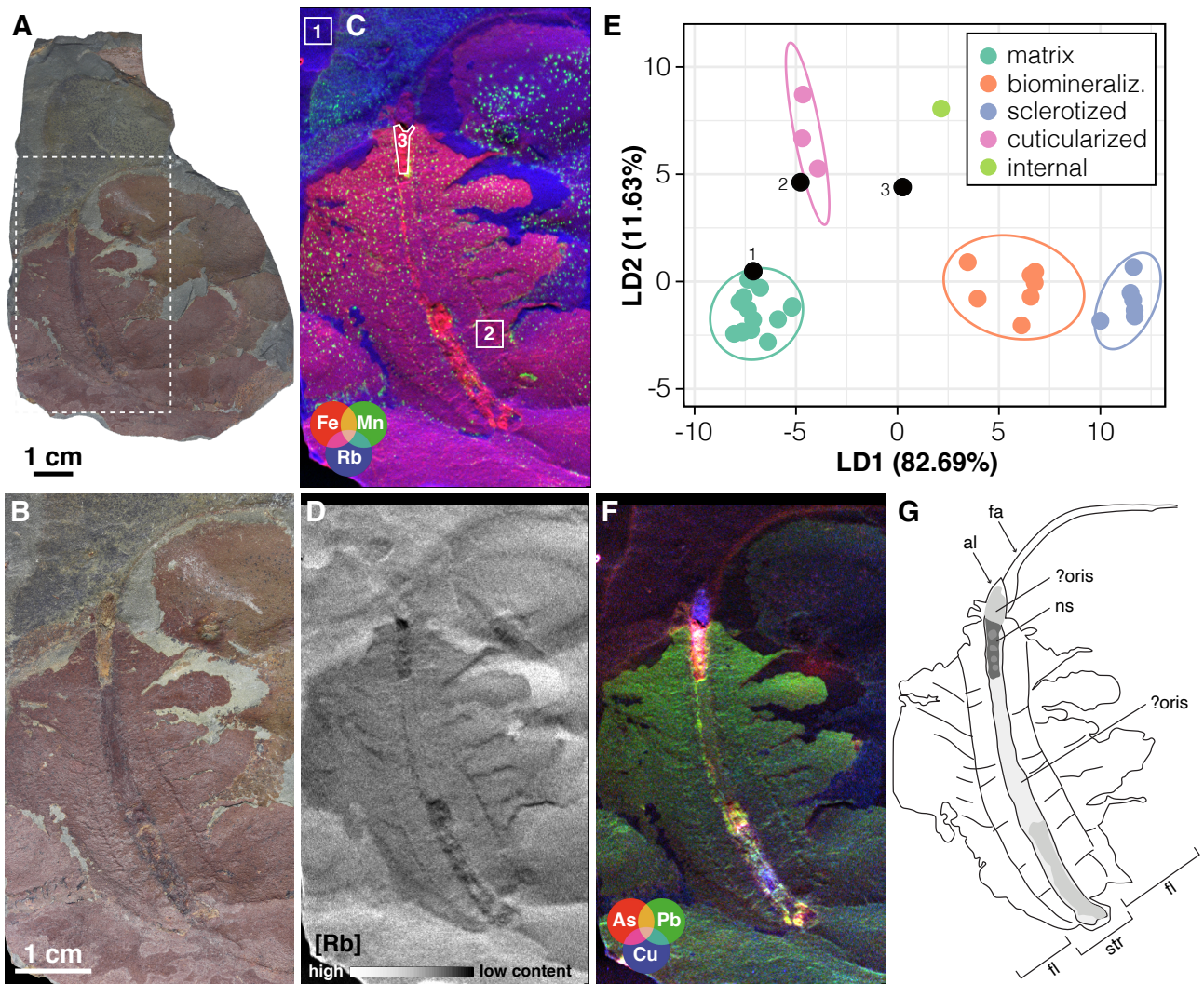
- 449 42. G. Tanaka, X. Hou, X. Ma, G. D. Edgecombe, N. J. Strausfeld, Chelicerate neural ground  
450 pattern in a Cambrian great appendage arthropod. *Nature* **502**, 364–367 (2013).
- 451 43. P. Cong, X. Ma, X. Hou, G. D., Edgecombe, N. J. Strausfeld, Brain structure resolves the  
452 segmental affinity of anomalocaridid appendages. *Nature* **513**, 538–542 (2014).
- 453 44. J. Yang, J. Ortega-Hernández, N. J. Butterfield, Y. Liu, G. S. Boyan, J.-b. Hou, T. Lan, X.-g.  
454 Zhang, Fuxianhuiid ventral nerve cord and early nervous system evolution in  
455 Panarthropoda. *Proc. Natl. Acad. Sci. U.S.A.* **113**, 2988–2993 (2016).
- 456 45. L. Parry, J. B. Caron, *Canadia spinosa* and the early evolution of the annelid nervous  
457 system. *Science advances* **5**, eaax5858 (2019).
- 458 46. T. Lan, Y. Zhao, F. Zhao, Y. He, P. Martinez, N. J. Strausfeld, Leanchoiliidae reveals the  
459 ancestral organization of the stem euarthropod brain. *Current Biology* **31**, 4397–4404  
460 (2021).
- 461 47. J. Ortega-Hernández, R. Lerosey-Aubril, S. R. Losso, J. C. Weaver, Neuroanatomy in a  
462 middle Cambrian mollisoniid and the ancestral nervous system organization of chelicerates.  
463 *Nature communications* **13**, 410 (2022).
- 464 48. N. J. Strausfeld, X. Hou, M. E. Sayre, F. Hirth, The lower Cambrian lobopodian  
465 *Cardiodictyon* resolves the origin of euarthropod brains. *Science* **378**, 905–909 (2022).
- 466 49. R. T. Figueroa, D. Goodvin, M. A. Kolmann, M. I. Coates, A. M. Caron, M. Friedman, S.  
467 Giles, Exceptional fossil preservation and evolution of the ray-finned fish brain. *Nature*  
468 (2023). <https://doi.org/10.1038/s41586-022-05666-1>.
- 469 50. F. Saleh, A. C. Daley, B. Lefebvre, B. Pittet, J. P. Perrillat, Biogenic iron preserves  
470 structures during fossilization: a hypothesis: iron from decaying tissues may stabilize their  
471 morphology in the fossil record. *BioEssays* **42**, 1900243 (2020).
- 472 51. C. Aria, J. Vannier, J., T. Y. S. Park, R. R. Gaines, Interpreting fossilized nervous tissues.  
473 *BioEssays* (2023). <https://doi.org/10.1002/bies.202200167>.
- 474 52. R. A. Wogelius, P. L. Manning, H. E. Barden, N. P. Edwards, S. M. Webb, W. I. Sellers, K.  
475 G. Taylor, P. L. Larson, P. Dodson, H. You, L. Da-qing, U. Bergmann, Trace metals as  
476 biomarkers for eumelanin pigment in the fossil record. *Science* **333**, 1622–1626 (2011).
- 477 53. V. M. Egerton, R. A. Wogelius, M. A., Norell, N. P. Edwards, W. I. Sellers, U. Bergmann,  
478 D. Sokaras, R. Alonso-Mori, K. Ignatyev, A. van Veelen, J. Anné, B. E. van Dongen, F.  
479 Knoll, P. L. Manning, The mapping and differentiation of biological and environmental  
480 elemental signatures in the fossil remains of a 50 million year old bird. *Journal of Analytical*  
481 *Atomic Spectrometry* **30**, 627–634 (2015).
- 482 54. P. L. Manning, N. P. Edwards, U. Bergmann, J. Anné, W. I. Sellers, A. van Veelen, D.  
483 Sokaras, V. M. Egerton, R. Alonso-Mori, K. Ignatyev, B. E. van Dongen, K. Wakamatsu, S.  
484 Ito, F. Knoll, R. A. Wogelius, Pheomelanin pigment remnants mapped in fossils of an  
485 extinct mammal. *Nature Communications* **10**, 2250 (2019).
- 486 55. V. Rossi, M. E. McNamara, S. M. Webb, S. Ito, K. Wakamatsu, Tissue-specific geometry  
487 and chemistry of modern and fossilized melanosomes reveal internal anatomy of extinct  
488 vertebrates. *Proc. Natl. Acad. Sci. U.S.A.* **116**, 17880–17889 (2019).
- 489 56. V. Rossi, S. M. Webb, M. E. McNamara, Hierarchical biota-level and taxonomic controls on  
490 the chemistry of fossil melanosomes revealed using synchrotron X-ray fluorescence.  
491 *Scientific Reports* **10**, 8970 (2020).

- 492 57. V. Rossi, S. M. Webb, M. E. McNamara, Maturation experiments reveal bias in the  
493 chemistry of fossil melanosomes. *Geology* **49**, 784–788 (2021).
- 494 58. A. Brayard, P. Gueriau, M. Thoury, G. Escarguel, the Paris Biota team, Glow in the dark:  
495 Use of synchrotron  $\mu$ XRF trace elemental mapping and multispectral macro-imaging on  
496 fossils from the Paris Biota (Bear Lake County, Idaho, USA). *Geobios* **54**, 71–79 (2019).
- 497 59. T. Saucède, E. Vennin, E. Fara, N. Olivier, the Paris Biota team, A new holocrinid  
498 (Articulata) from the Paris Biota (Bear Lake County, Idaho, USA) highlights the high  
499 diversity of Early Triassic crinoids. *Geobios* **54**, 45–53 (2019).
- 500 60. P. Gueriau, J. C., Lamsdell, R. A. Wogelius, P. L. Manning, V. M. Egerton, U. Bergmann,  
501 L. Bertrand, J. Denayer, A new Devonian euthycarcinoid evidences the use of different  
502 respiratory strategies during the marine-to-terrestrial transition in the myriapod lineage.  
503 *Royal Society Open Science* **7**, 201037 (2020).
- 504 61. N. Leclercq, J. Berthault, F. Langlois, S. Le, S. Poirier, J. Bisou, F. Blache, K. Medjoubi, C  
505 Mocuta, Flyscan: a fast and multi-technique data acquisition platform for the SOLEIL  
506 beamlines. *ICALPCS 2015, the 15th International Conference on Accelerator and Large*  
507 *Experimental Control Systems*, 17–23 October 2015, Melbourne, Australia, Abstract No.  
508 WEPGF056 (2015).
- 509 62. W. N. Venables, B. D. Ripley, *Modern Applied Statistics with S* (Springer-Verlag New  
510 York, 2002).
- 511 63. H. Wickham, *ggplot2: Elegant Graphics for Data Analysis* (Springer-Verlag New York,  
512 2016).
- 513 64. C. Beleites, V. Sergo, hyperSpec: a package to handle hyperspectral data sets in R, *R*  
514 *package version 0.99-20201127*. (<https://github.com/cbeleites/hyperSpec>) (2020).
- 515 65. P. Gueriau, C. Mocuta, L. Bertrand, Cerium anomaly at microscale in fossils. *Analytical*  
516 *Chemistry* **87**, 8827–8836 (2015).
- 517 66. P. Gueriau, S. Bernard, F. Farges, C. Mocuta, D. B. Dutheil *et al.*, Oxidative conditions can  
518 lead to exceptional preservation through phosphatization. *Geology* **48**, 1164–1168 (2020).
- 519 67. V. A. Solé, E. Papillon, M. Cotte, P. Walter, J. Susini, A multiplatform code for the analysis  
520 of energy-dispersive X-ray fluorescence spectra. *Spectrochimica Acta Part B: Atomic*  
521 *Spectroscopy* **62**, 63–68 (2007).
- 522





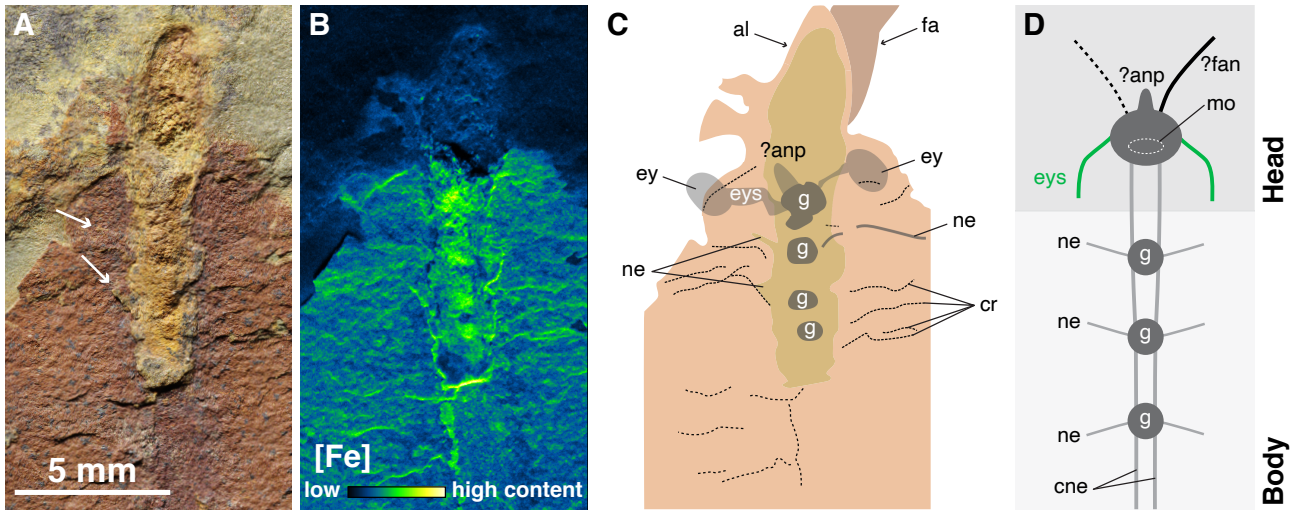
523  
 524 **Figure 1. Synchrotron-based XRF major-to-trace elemental mapping of 14 fossil animals from**  
 525 **the Early Ordovician Fezouata Shale of Morocco.** (A–M) Optical photograph and false-colour  
 526 overlays of iron (red), manganese (green), and rubidium (blue) distributions of the analysed fossils  
 527 (see Table S1 for specimen details and acquisition parameters). (N) Linear discriminant analysis of  
 528 the mean XRF spectra extracted from the white box areas in A–M; white arrows locate spectra for  
 529 the shale matrix that were taken outside of the displayed field of view, their length being  
 530 proportional to the distance from the sampled area (see Figs. S1–S14 for precise locations). (O)  
 531 Mean XRF spectrum for each tissue type and the matrix, vertically shifted for readability. The  
 532 ‘Fe ×2’ peak in the fossil spectra corresponds to a Fe pile-up peak, an artefactual peak<sup>36</sup> that  
 533 increases with concentration and further indicate that fossil tissues are richer in Fe than the shale.  
 534 **[planned for 2-column width]**



535  
 536 **Figure 2. Synchrotron-based XRF major-to-trace elemental mapping of a highly weathered**  
 537 **organism (AA-FETB-OI-22) from the Early Ordovician Fezouata Shale of Morocco.** (A)  
 538 Optical photograph of the entire slab. (B) Close-up on the specimen, from the dotted white box area  
 539 in A. (C) False-colour overlay of iron (red), manganese (green), and rubidium (blue) distributions  
 540 from the area in B. Acquisition parameters: 100×100 μm<sup>2</sup> scan step, 20 ms dwell time, 215 280  
 541 pixels. Numbered white box areas indicate location of XRF spectra in E. (D) Rubidium distribution  
 542 only. (E) Classification of the mean XRF spectra extracted from the white box areas in C within our  
 543 LDA. (F) False-colour overlay of arsenic (red), lead (green), and copper (blue) distributions. (G)  
 544 Interpretative line drawing of the anatomy of the specimen. Abbreviations: al, anterior lobe; fa,  
 545 frontal appendage; fl, lateral flaps; ns, nervous system; ?oris, other remains of internal system(s);  
 546 str, segmented trunk.

547 **[planned for 2-column width]**

548



549  
 550 **Figure 3. Remains of the nervous system in AA-FETB-OI-22.** (A) Close-up optical photograph  
 551 of the head and anteriormost portion of the body. Arrows highlight lateral extensions of the  
 552 yellowish region. (B) Iron distribution (XRF contrast map). Acquisition parameters:  $25 \times 25 \mu\text{m}^2$   
 553 scan step, 20 ms dwell time, 264 163 pixels. (C) Interpretative line drawing. (D) Schematic  
 554 reconstructed of the nervous system. Abbreviations: al, anterior lobe; anp, anterior neural  
 555 projection, cne, central nerves, cr, cracks; ey, eye; eys, eye stalk; g, ganglion; fa, frontal appendage;  
 556 fan, frontal appendage nerves; mo, mouth; ne, nerves.

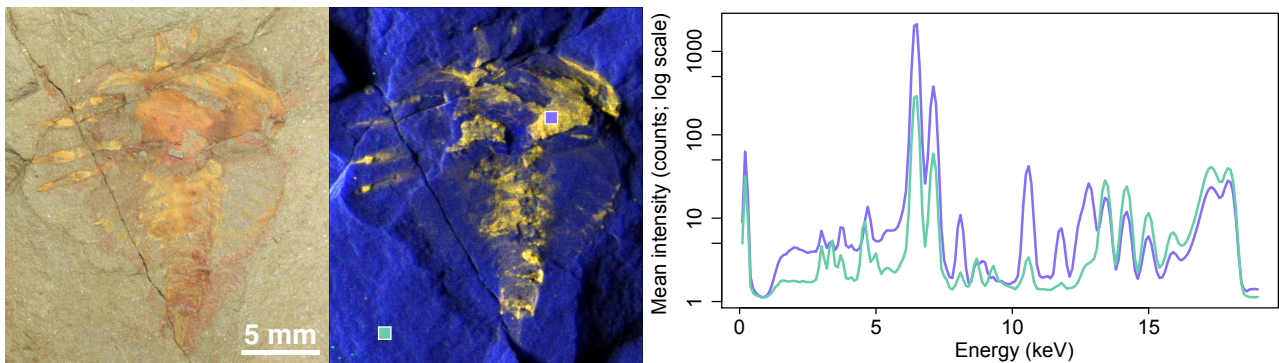
557 **[planned for 2-column width]**

558  
 559

560 **Extended Data Figures.**

561

562



563

564

565

566

567

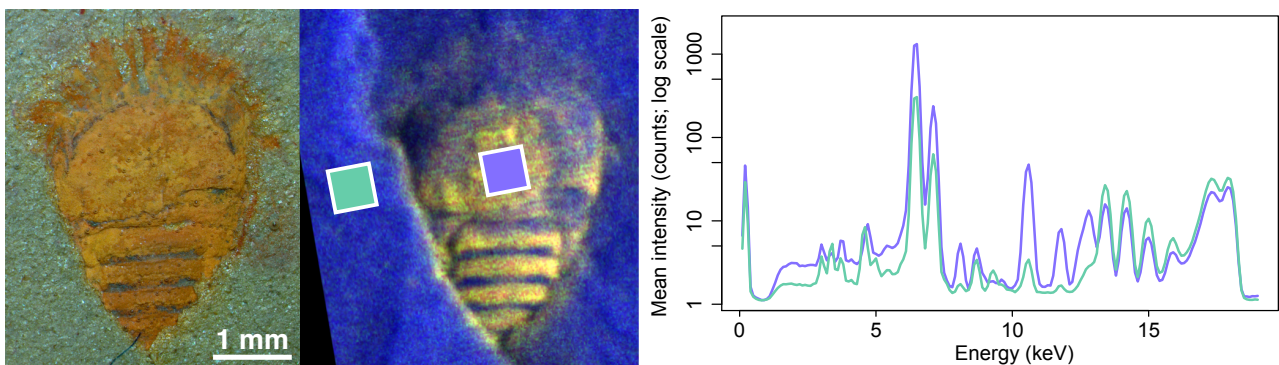
568

569

570

571

**Figure S1. Synchrotron-based XRF major-to-trace elemental mapping of MGL 102701, an undescribed “xiphosuran” from the Early Ordovician Fezouata Shale of Morocco.** Optical photograph (*left*), false-colour overlays of iron (red), manganese (green), and rubidium (blue) distributions (*centre*), and the extracted mean XRF spectra from box areas of corresponding colours in the elemental overlay (*right*). Refer to Fig. 1O for peak identification.



572

573

574

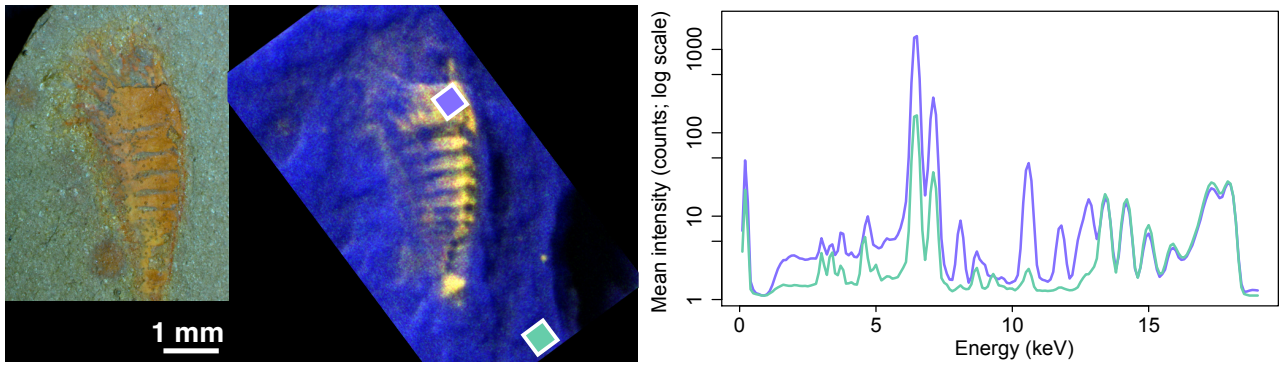
575

576

577

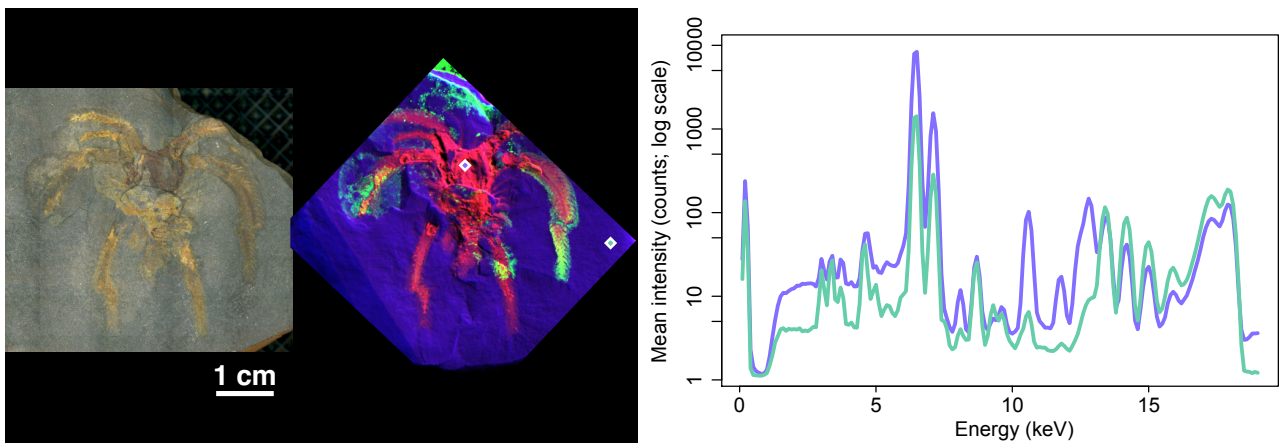
578

**Figure S2. Synchrotron-based XRF major-to-trace elemental mapping of MGL 107210, an undescribed “synziphosurine” from the Early Ordovician Fezouata Shale of Morocco.** Optical photograph (*left*), false-colour overlays of iron (red), manganese (green), and rubidium (blue) distributions (*centre*), and the extracted mean XRF spectra from box areas of corresponding colours in the elemental overlay (*right*). Refer to Fig. 1O for peak identification.



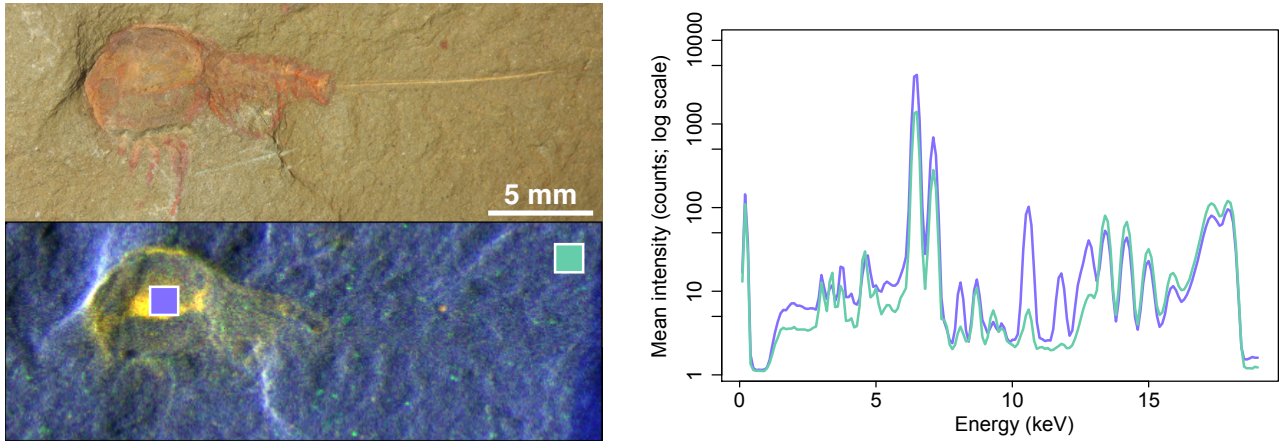
579  
580  
581  
582  
583  
584  
585  
586  
587  
588

**Figure S3. Synchrotron-based XRF major-to-trace elemental mapping of MGL 102841, an undescribed "synziphosurine" from the Early Ordovician Fezouata Shale of Morocco.** Optical photograph (*left*), false-colour overlays of iron (red), manganese (green), and rubidium (blue) distributions (*centre*), and the extracted mean XRF spectra from box areas of corresponding colours in the elemental overlay (*right*). Refer to Fig. 1O for peak identification.



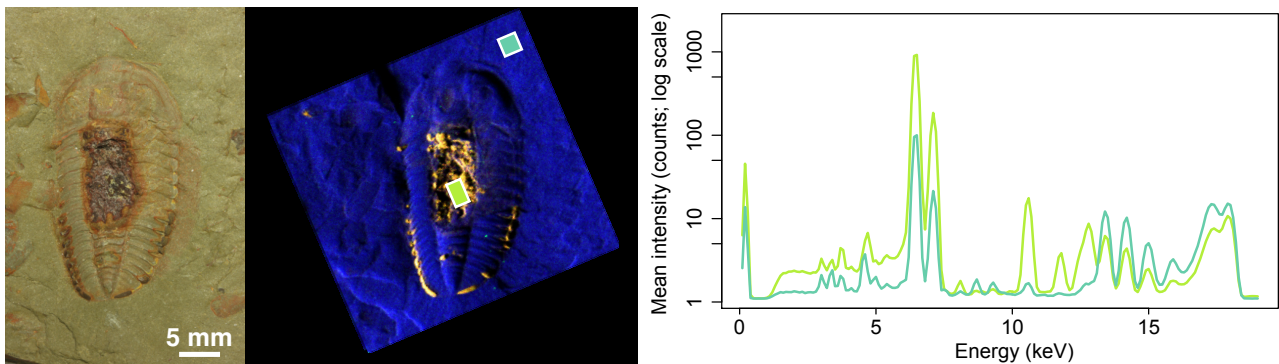
589  
590  
591  
592  
593  
594  
595

**Figure S4. Synchrotron-based XRF major-to-trace elemental mapping of AA-BIZ31-OI-39, an undescribed "marrellid" from the Early Ordovician Fezouata Shale of Morocco.** Optical photograph (*left*), false-colour overlays of iron (red), manganese (green), and rubidium (blue) distributions (*centre*), and the extracted mean XRF spectra from box areas of corresponding colours in the elemental overlay (*right*). Refer to Fig. 1O for peak identification.



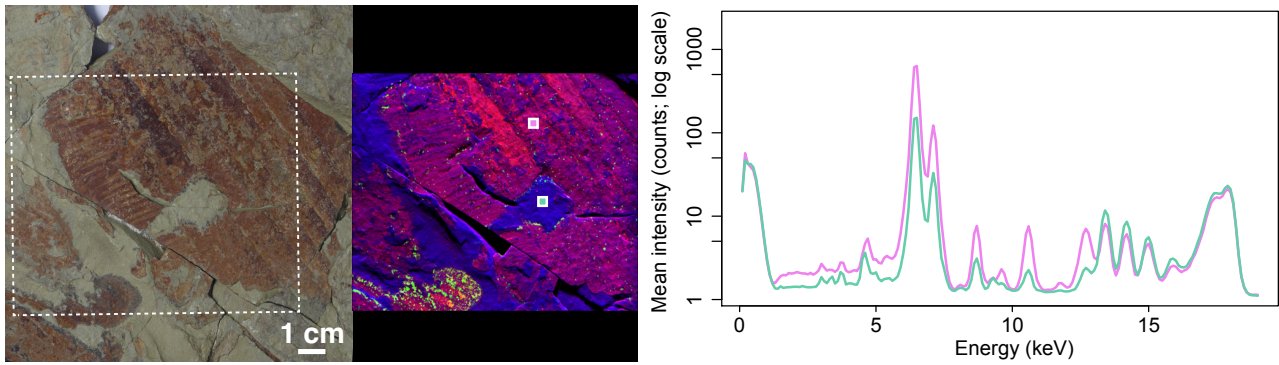
596  
 597 **Figure S5. Synchrotron-based XRF major-to-trace elemental mapping of MGL 102705, an**  
 598 **undescribed “xiphosuran” from the Early Ordovician Fezouata Shale of Morocco.** Optical  
 599 photograph (*top left*), false-colour overlays of iron (red), manganese (green), and rubidium (blue)  
 600 distributions (*bottom left*), and the extracted mean XRF spectra from box areas of corresponding  
 601 colours in the elemental overlay (*right*). Refer to Fig. 1O for peak identification.

602  
 603  
 604  
 605



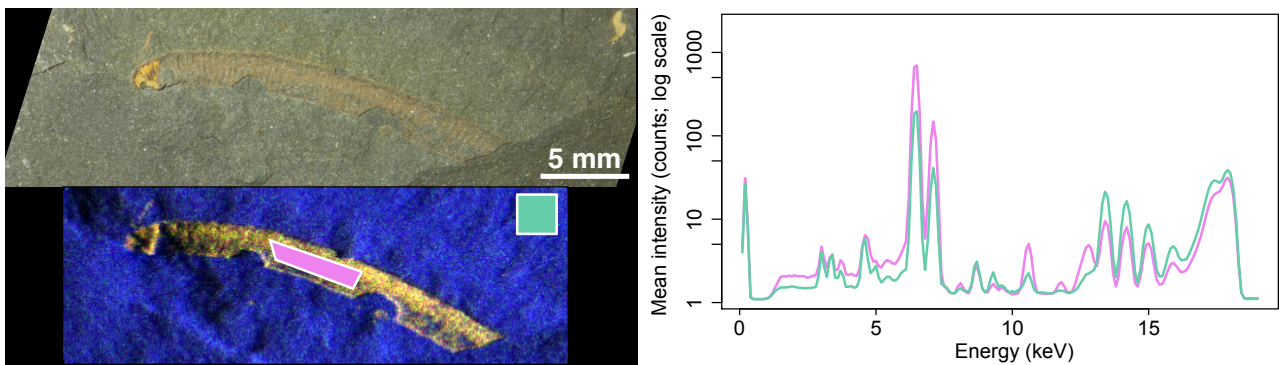
606  
 607 **Figure S6. Synchrotron-based XRF major-to-trace elemental mapping of the trilobite**  
 608 ***Bavarilla zemmourensis* Destombes, Sougy & Willefert, 1969, specimen MGL 102177, from the**  
 609 **Early Ordovician Fezouata Shale of Morocco.** Optical photograph (*left*), false-colour overlays of  
 610 iron (red), manganese (green), and rubidium (blue) distributions (*centre*), and the extracted mean  
 611 XRF spectra from box areas of corresponding colours in the elemental overlay (*right*). Refer to Fig.  
 612 1O for peak identification.

613



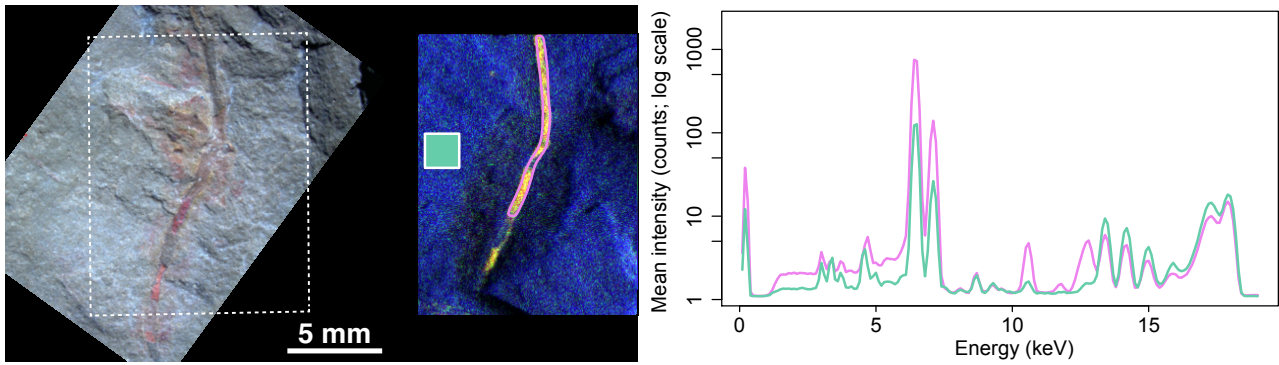
614  
 615 **Figure S7. Synchrotron-based XRF major-to-trace elemental mapping of MGL 103593,**  
 616 **undescribed "radiodont" appendages from the Early Ordovician Fezouata Shale of Morocco.**  
 617 Optical photograph (*left*), false-colour overlays of iron (red), manganese (green), and rubidium  
 618 (blue) distributions (*centre*), and the extracted mean XRF spectra from box areas of corresponding  
 619 colours in the elemental overlay (*right*). Refer to Fig. 1O for peak identification.

620  
 621  
 622  
 623



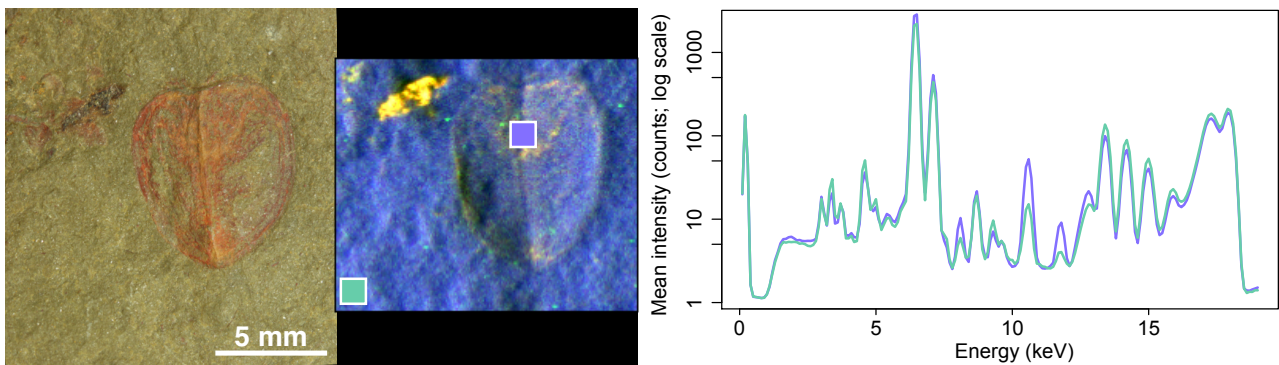
624  
 625 **Figure S8. Synchrotron-based XRF major-to-trace elemental mapping of MGL 107866, an**  
 626 **undescribed "annelid" from the Early Ordovician Fezouata Shale of Morocco.** Optical  
 627 photograph (*top left*), false-colour overlays of iron (red), manganese (green), and rubidium (blue)  
 628 distributions (*bottom left*), and the extracted mean XRF spectra from box areas of corresponding  
 629 colours in the elemental overlay (*right*). Refer to Fig. 1O for peak identification.

630



631  
632  
633  
634  
635  
636  
637  
638  
639  
640

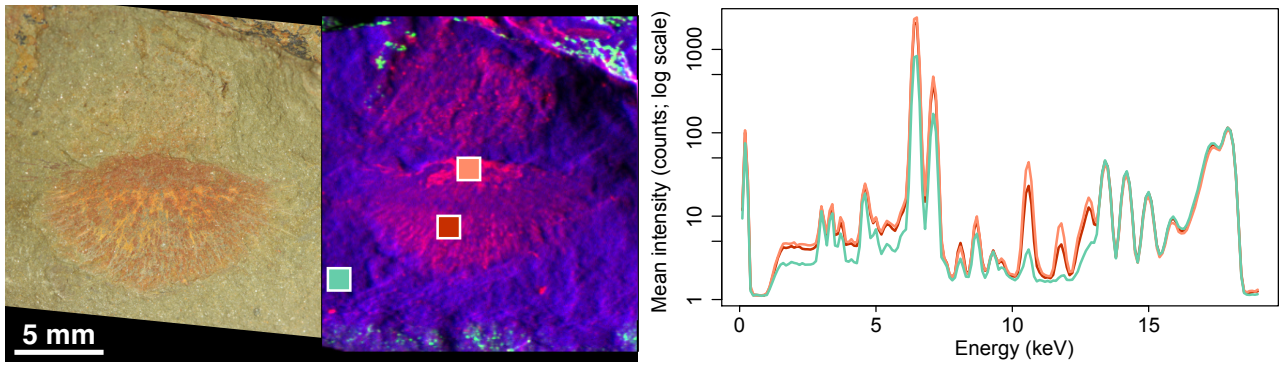
**Figure S9. Synchrotron-based XRF major-to-trace elemental mapping of AA-TGR1c-OI-47, an undescribed "annelid" from the Early Ordovician Fezouata Shale of Morocco.** Optical photograph (*left*), false-colour overlays of iron (red), manganese (green), and rubidium (blue) distributions (*centre*), and the extracted mean XRF spectra from selected areas of corresponding colours in the elemental overlay (*right*). Refer to Fig. 10 for peak identification.



641  
642  
643  
644  
645  
646  
647  
648

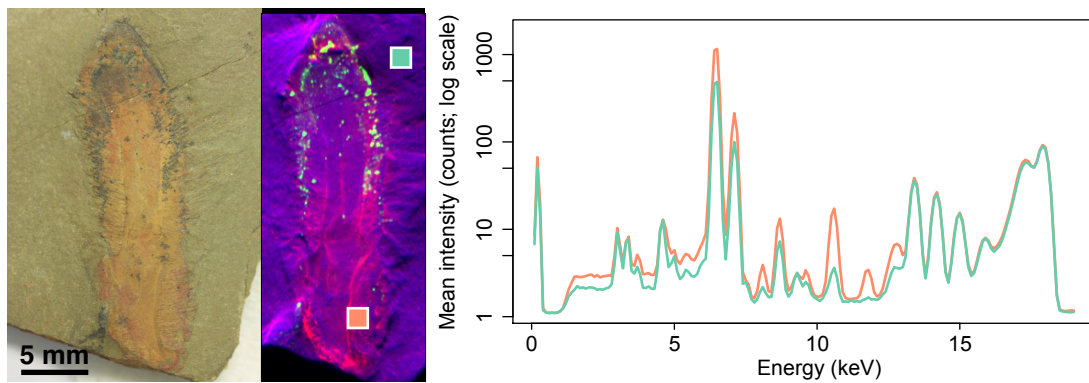
**Figure S10. Synchrotron-based XRF major-to-trace elemental mapping of the marrellomorph euarthropod *Enosiaspis hrungnir* Legg, 2016, specimen MGL 102321, from the Early Ordovician Fezouata Shale of Morocco.** Optical photograph (*left*), false-colour overlays of iron (red), manganese (green), and rubidium (blue) distributions (*centre*), and the extracted mean XRF spectra from box areas of corresponding colours in the elemental overlay (*right*). Refer to Fig. 10 for peak identification.





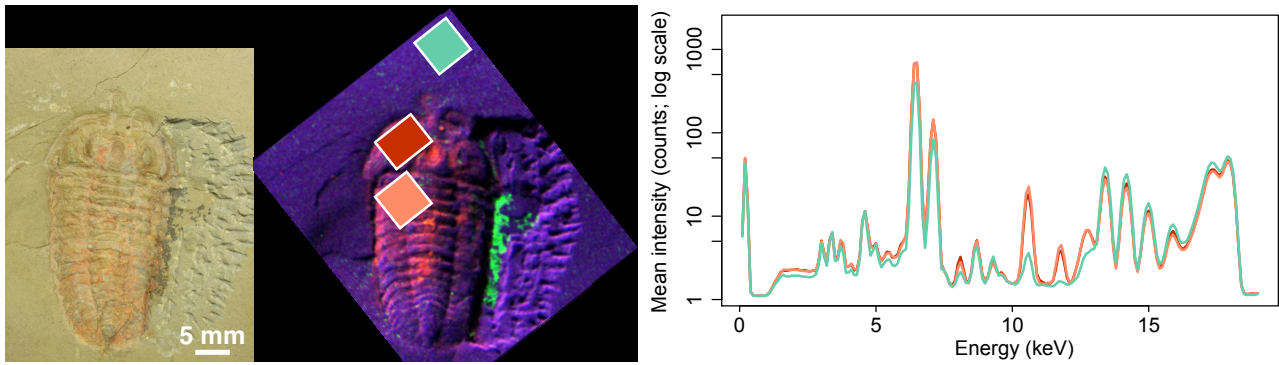
649  
 650 **Figure S11. Synchrotron-based XRF major-to-trace elemental mapping of the demosponge**  
 651 ***Choia sp.*, specimen MGL 107663, from the Early Ordovician Fezouata Shale of Morocco.**  
 652 Optical photograph (*left*), false-colour overlays of iron (red), manganese (green), and rubidium  
 653 (blue) distributions (*centre*), and the extracted mean XRF spectra from box areas of corresponding  
 654 colours in the elemental overlay (*right*). Refer to Fig. 1O for peak identification.

655  
 656  
 657  
 658



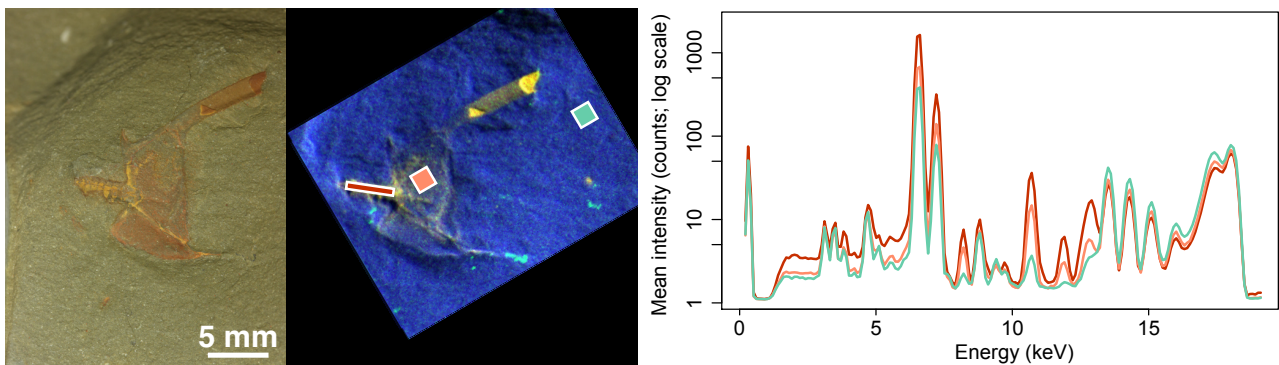
659  
 660 **Figure S12. Synchrotron-based XRF major-to-trace elemental mapping of the demosponge**  
 661 ***Pirania auraeum* Botting, 2007, specimen MGL 107764, from the Early Ordovician Fezouata**  
 662 **Shale of Morocco.** Optical photograph (*left*), false-colour overlays of iron (red), manganese  
 663 (green), and rubidium (blue) distributions (*centre*), and the extracted mean XRF spectra from box  
 664 areas of corresponding colours in the elemental overlay (*right*). Refer to Fig. 1O for peak  
 665 identification.

666



667  
 668 **Figure S13. Synchrotron-based XRF major-to-trace elemental mapping of the trilobite**  
 669 ***Bavarilla zemmourensis* Destombes, Sougy & Willefert, 1969, specimen MGL 102222, from the**  
 670 **Early Ordovician Fezouata Shale of Morocco.** Optical photograph (*left*), false-colour overlays of iron (red), manganese (green), and rubidium (blue) distributions (*centre*), and the extracted mean  
 671 XRF spectra from box areas of corresponding colours in the elemental overlay (*right*). Refer to Fig.  
 672 1O for peak identification.  
 673

674  
 675  
 676  
 677

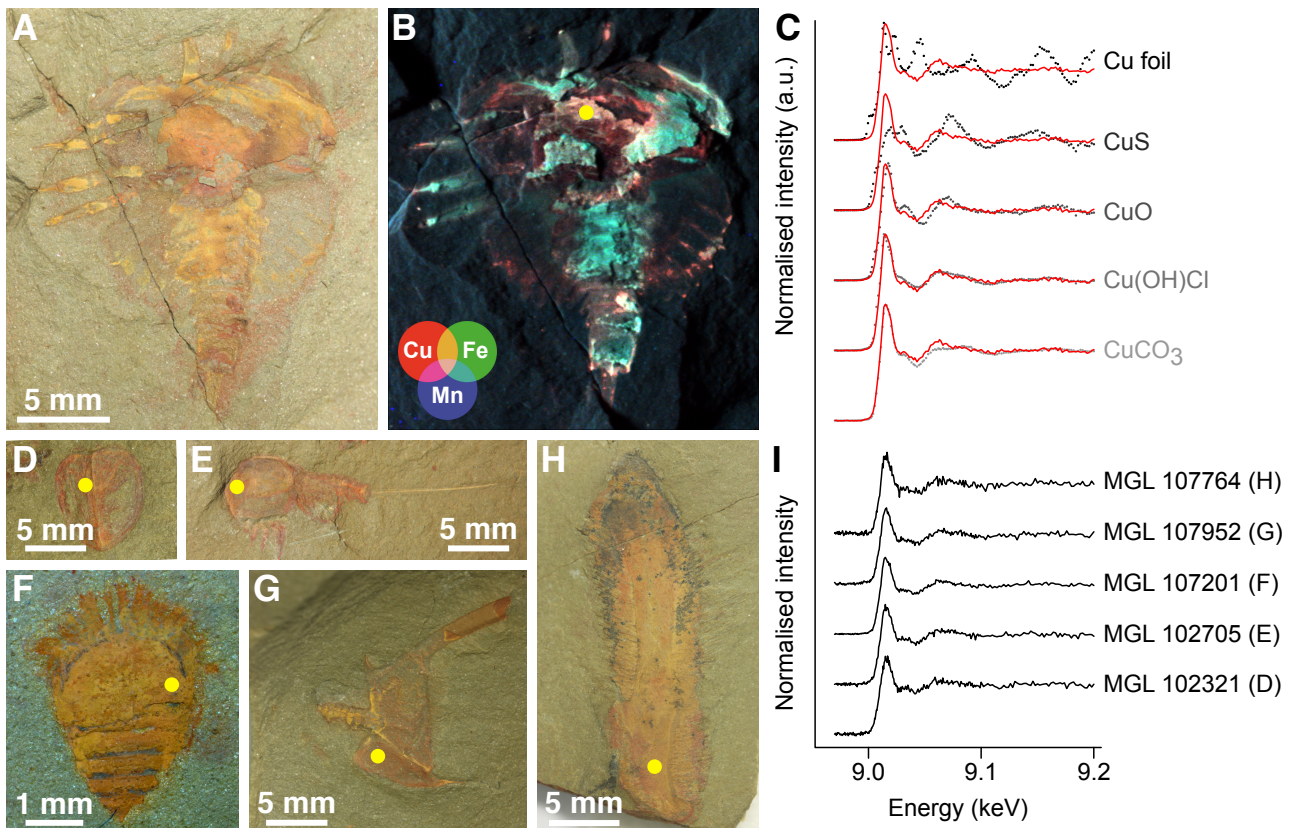


678  
 679 **Figure S14. Synchrotron-based XRF major-to-trace elemental mapping of the stylophoran**  
 680 **echinoderm *Thoralicystis* sp., specimen MGL 107952, from the Early Ordovician Fezouata**  
 681 **Shale of Morocco.** Optical photograph (*left*), false-colour overlays of iron (red), manganese  
 682 (green), and rubidium (blue) distributions (*centre*), and the extracted mean XRF spectra from box  
 683 areas of corresponding colours in the elemental overlay (*right*). Refer to Fig. 1O for peak  
 684 identification.  
 685

685

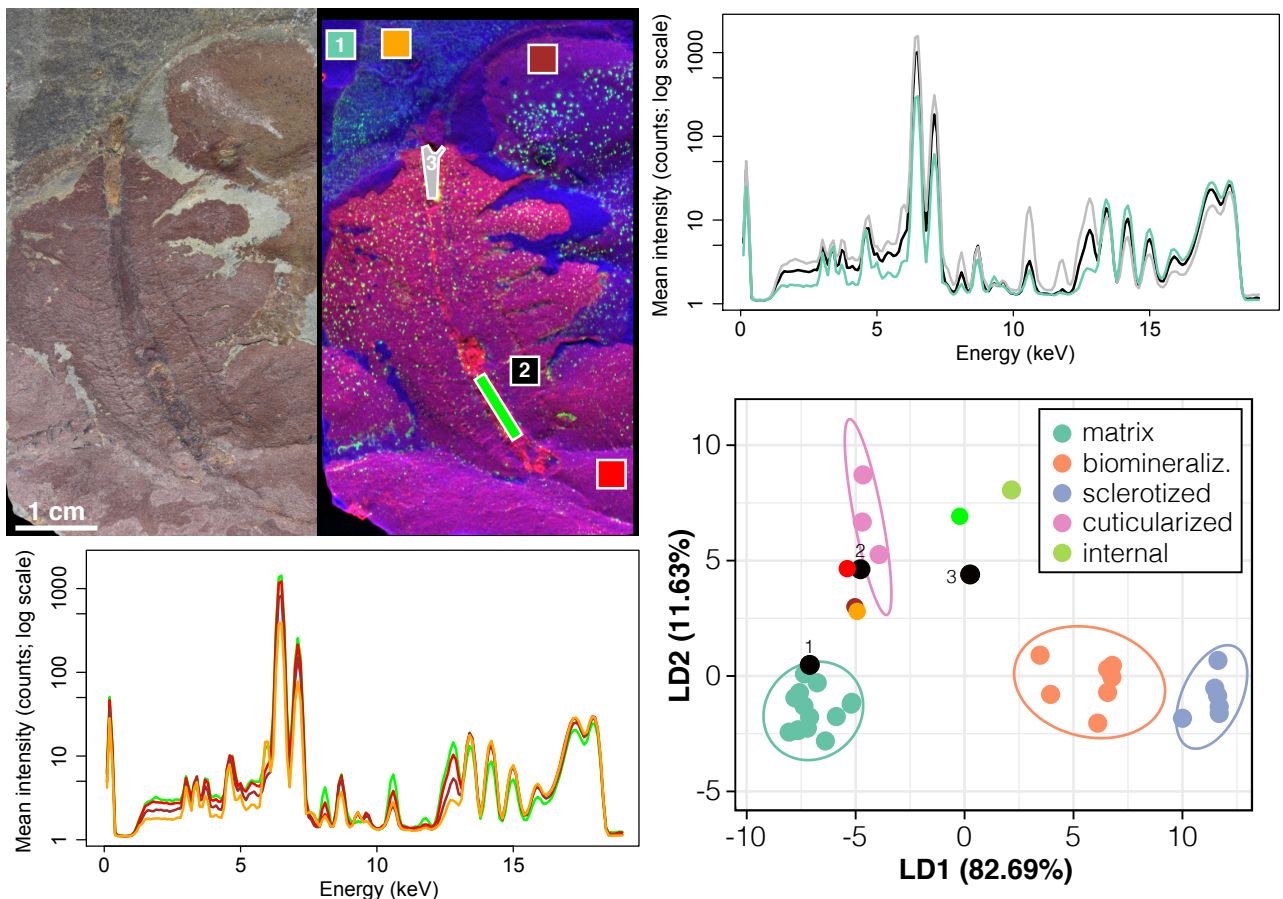


686  
 687 **Figure S15. Satellite view of the Draa valley locating the different outcrops that yielded the**  
 688 **fossils studied herein.** The '~14km' measurement refers to the perimeter encompassing all the  
 689 north localities. Precise locality information is curated with the specimens, and available upon  
 690 request from the authors.  
 691



692  
 693 **Figure S16. Synchrotron-based Cu K-edge X-ray absorption spectroscopy (XAS) of a range of**  
 694 **fossils from the Early Ordovician Fezouata Shale of Morocco.** (A) Optical photograph of the  
 695 undescribed "xiphosuran" MGL 102701. (B) false-colour overlays of copper (red), iron (green), and  
 696 manganese (blue) distributions. (C) Cu K-edge XAS spectrum (red line) from the yellow dot in B  
 697 superimposed upon spectra collected on reference Cu compounds (grey to black dotted lines) for  
 698 comparison. The spectrum obtained for the fossil is inconsistent with metallic copper (Cu), copper  
 699 sulfide (CuS) or cupric oxide (CuO) but more consistent with copper hydroxide chloride  
 700 (Cu(OH)Cl) and to a greater extent copper carbonate (CuCO<sub>3</sub>), suggesting a similar environment for  
 701 Cu in the fossil. (D–H) Optical photographs of *Enosiaspis hrungnir* MGL 102321 (D), the  
 702 undescribed "xiphosuran" MGL 102705 (E), the undescribed "synziphosurine" MGL 107210 (F),  
 703 *Thoralicystis sp.* MGL 107952 (G), and *Pirania auraeum* MGL 107764 (H). (I) Cu K-edge XAS  
 704 spectra from the yellow dot in D–H, showing that Cu is present in all investigated fossils in the  
 705 same chemical environment. XAS was performed at the DiffAbs beamline (SOLEIL synchrotron)  
 706 with the following acquisition parameters: fluorescence mode, 230×150 μm<sup>2</sup> (H×V) beam spot size,  
 707 3 s counting time per energy step; energy step sizes were 0.5 eV between 8970 and 9030 eV, 1 eV  
 708 between 9031 and 9100 eV, and 2 eV between 9102 and 9200 eV. Spectra have been normalised,  
 709 and the references corrected from self-absorption, using the Athena software<sup>68</sup>.

710  
 711 68. B. Ravel, M. Newville, ATHENA, ARTEMIS, HEPHAESTUS: data analysis for X-ray  
 712 absorption spectroscopy using IFEFFIT. *Journal of Synchrotron Radiation* **12**, 537–541  
 713 (2005).  
 714



715  
 716 **Figure S17. Synchrotron-based X-ray fluorescence major-to-trace elemental mapping of AA-**  
 717 **FETB-OI-22, an undescribed “enigmatic organism” from the Early Ordovician Fezouata**  
 718 **Shale of Morocco.** (Top left) Optical photograph. (Top centre) False-colour overlays of iron (red),  
 719 manganese (green), and rubidium (blue) distributions. (Top right) Mean XRF spectra from the box  
 720 areas of corresponding colours (numbered 1 to 3) in the elemental overlay, corresponding to the  
 721 same areas as in Fig. 2C. (Bottom left) Additional mean XRF spectra, extracted from the orange,  
 722 brown, red (weathered matrix) and green (other internal remains) box areas of corresponding  
 723 colours in the XRF false-colour overlay. Refer to Fig. 10 for peak identification. (Bottom right)  
 724 Classification of the all 7 extracted XRF spectra within our linear discriminant analysis. Note that  
 725 weathered matrix spectra plot closer to cuticularized tissues the richer they are in iron, following the  
 726 fact that the shale matrix (clay and silica) is way less concentrated in iron than the fossil tissues  
 727 (iron oxides). Of note is also the classification of the green XRF spectrum, corresponding to the  
 728 remains of an internal system, which plots close to the trilobite internal, most likely digestive,  
 729 tissue, suggesting that this area may preserve remains of the digestive system.  
 730  
 731

Taxon	Collection number	Locality	Figure(s)	Spectrum	Tissue type (Following [35])	XRF map scan step ( $\mu\text{m}$ )	XRF map dwell time (ms)	Number of pixels selected	Time over slected area (s)
undescribed "xiphosuran"	MGL 102701	A5 (2015)	Figs. 1A, S1	1	sclerotised	20	25	900	22.5
				2	matrix	20	25	900	22.5
undescribed "synziphosurine"	MGL 107210	A16 (2015)	Figs. 1B, S2	1	sclerotised	20	20	1122	22.44
				2	matrix	20	20	1122	22.44
undescribed "synziphosurine"	MGL 102841	"Synz. Loc."	Figs. 1C, S3	1	sclerotised	20	20	1122	22.44
				2	matrix	20	20	1122	22.44
undescribed "marrellid"	AA-BIZ31-OI-39	ZF4(31)	Figs. 1D, S4	1	sclerotised	70	70	324	22.68
				2	matrix	70	70	324	22.68
undescribed "xiphosuran"	MGL 102705	A5 (2015)	Figs. 1E, S5	1	sclerotised	70	50	441	22.05
				2	matrix	70	50	441	22.05
<i>Bavarilla zemmourensis</i> Destombes. Sougy & Willefert. 1969	MGL 102177	A17 (2015)	Figs. 1F, S6	1	internal	70	20	1128	22.56
				2	matrix	70	20	1122	22.44
undescribed "radiodont" appendages	MGL 103593	A27 (2016)	Figs. 1G, S7	1	cuticularised	70	25	900	22.5
				2	matrix	70	25	900	22.5
undescribed "annelid"	MGL 107866	A2 (2015)	Figs. 1H, S8	1	cuticularised	70	20	1127	22.54
				2	matrix	70	20	1122	22.44
undescribed "annelid"	AA-TGR1c-OI-47	ZF51c	Fig. S9	1	cuticularised	70	20	1124	22.48
				2	matrix	70	20	1122	22.44
<i>Enosiaspis hrungnir</i> Legg. 2016	MGL 102321	A6 (2015)	Figs. 1I, S10	1	sclerotised	70	60	380	22.8
				2	matrix	70	60	380	22.8
<i>Choia</i> sp. (Botting 2007)	MGL 107663	A17 (2015)	Figs. 1J, S11	1	biomineralised	70	50	441	22.05
				2	biomineralised	70	50	441	22.05
				3	matrix	70	50	441	22.05
<i>Pirania auraeum</i> Botting. 2007	MGL 107764	A26 (2016)	Figs. 1K, S12	1	biomineralised	70	40	552	22.08
				2	matrix	70	40	552	22.08

<i>Bavarilla zemmourensis</i> Destombes. Sougy & Willefert. 1969	MGL 102222	A16 (2015)	Figs. 1L, S13	1	biomineralised	200	20	1122	22.44
				2	biomineralised	200	20	858	17.16 **
				3	matrix	200	20	1122	22.44
<i>Thoralicystis</i> sp. (Lefebvre et al. 2019)	MGL 107952	A9 (2015)	Figs. 1M, S14	1	biomineralised	70	30	729	21.87
				2	biomineralised	70	30	638	19.14 **
				3	matrix	70	30	729	21.87
undescribed "enigmatic organism"	AA-FETB-OI-22	ZF2(3b)	Figs. 2, S17	1	?	100	20	1122	22.44
				2	?	100	20	1124	22.48
				3	matrix	100	20	1122	22.44
				4	weathered matrix	100	20	1122	22.44
				5	weathered matrix	100	20	1122	22.44
				6	weathered matrix	100	20	1122	22.44
				7	?	100	20	1121	22.42

**Table S1.** Details on the specimens. acquisition parameters and selected spectra studied herein. (\*\* Denotes 2 spectra for which it was not possible to obtain a collection time over the selected area close to 22.5 s)

Element	Sclerotised	Biom mineralised	Cuticularised
K	0.5112	1.956	0.4588
Ca	0.5725	0.5226	0.3237
Ti	0.1771	0.8605	0.2255
Cr	0.03413	0.04596	0.03328
Mn	0.2118	0.2076	0.2984
Ni	0.03054	0.03625	0.08007
Cu	0.3035	0.2087	0.02415
Zn	0.2127	0.4004	0.2436
Ga	0.007206	0.05585	0.01741
As	0.6792	0.522	0.04578
Br	0.006563	0.00397	0.0003272
Rb	0.2398	0.4184	0.1613
Sr	0.1391	0.2448	0.09511
Y	0.007973	0.03406	0.01968
Pb	0.5217	0.3441	0.3683

732

733

734

735

**Table S2.** XRF minor to trace element quantification of the mean spectra for the sclerotized, biom mineralized and cuticularized tissues (wt%)